Università degli Studi di Padova

Dipartimento di Fisica e Astronomia "Galileo Galilei"

Master degree in Astrophysics and Cosmology

FINAL DISSERTATION

Multiple populations among very low mass stars in 47 Tucanae

Supervisor:
Prof. Antonino MILONE

Candidate:
Sarah BAIMUKHAMETOVA

Academic Year 2022/2023

Abstract

Most Globular Clusters (GCs) host two main stellar populations. The so-called first-generation stars, which share the chemical composition of halo field stars with similar metallicity, and the second generations, which are composed of stars enhanced in He, N, Al and Na and depleted in C and O. Understanding the origin of the GCs and their multiple stellar populations is one of the main open issues in astrophysics. According to the main scenarios, the GCs has experienced a complex star-formation history with the formation of multiple generations of stars. These scenarios predict that the GCs were much more massive at formation and lost a large amount of mass into the field, thus providing a significant contribution to the assembly of the Galactic halo and, possibly, to the reionization of the Universe. As an alternative, all GC stars are coeval, and the specific chemical composition of the 2G stars is due to accretion onto pre-existing stars of material polluted by the ejecta of massive stars.

In this thesis, I analyzed deep multi-band Hubble Space Telescope images of two fields located in the outskirts of the massive GC 47 Tucanae. While previous works are mostly based on the most-massive GC stars, I explored the bottom of the main sequence. The IR color magnitude diagrams (CMDs) reveal that the MS region from the knee towards the H-burning limit exhibits a wide color spread, which is associated with star-to-star oxygen variations. By comparing the observed CMDs with appropriate isochrones, I infer the oxygen abundance of different stellar populations and find that the maximum oxygen variation among M-dwarfs is comparable to that derived for red-giant branch (RGB) stars by means of high-resolution spectroscopy. I constructed the pseudo two-color diagram dubbed chromosome map, which allowed me to disentangle the bulk of first- and second-generation stars. I found that the fraction of second-generation stars among the M-dwarfs is comparable to that observed among RGB stars at the same radial distances. Moreover, when I combine the results from this work with literature results based on the cluster center, I confirm that second generation stars are more centrally concentrated that the first generation. The radial distribution of the second generation and the evidence that the multiple population share similar chemical composition and relative numbers among stars with different masses (i.e. RGB and M-dwarfs) is in agreement with the prediction of the multi-generation scenarios, and challenge the scenarios based on accretion.

Contents

List of Figures

1 Introduction

The globular clusters (GCs) are spherical, stable, gravitationally bound aggregation of stars, found in all types of galaxies. These dense objects, which are typically composed of old stars, are of high scientific interest since they can further our understanding of stellar evolution, galactic dynamic, formation of galaxies and more.

After the formation of the cosmic microwave background the Universe was opaque, consisting of dense neutral Hydrogen. With time and under effects of gravity the gas started to clump, eventually leading to regions of high density. These regions cooled down and collapsed leading to the formation of stars, igniting nuclear fusion. The ultraviolet light from first stars ionized the Hydrogen gas, marking the beginning of the Reionization Epoch. GCs, being some of the oldest objects in the Universe, could potentially make a significant impact onto the reionization of the Universe.

The GCs formed during the early stages of galaxy formation, making them *relics* from the Early Universe useful to estimate the age of the Universe. They are typically found in the halo of their parent galaxies and resemble strong ties to their hosts. Thus, the physical properties of GCs like age, chemical composition, mass, and density distribution can shed light on the mechanisms, responsible for the assembly of galaxies.

1.1 Multiple Populations

In the past GCs were considered prototypes of Simple Stellar Populations (SSPs, e.g. Renzini & Buzzoni 1986), which are defined as groups of coeval stars with the same chemical composition. Thus, GCs were considered laboratories to test theories of star formation and evolution. However the discovery of multiple stellar populations in GCs challenged the SSP assumption. This revelation was possible due to improvements in instrumentation and photometry.

There were several observational phenomena, challenging the SSP assumption (Milone & Marino, 2022):

- **Chemical anomalies** The chemical composition of stars in most GCs is not homogeneous. Indeed, it is well known since the sixties that GCs exhibit star-to-star variations in the abundances of elements involved in hot Hydrogen burning processes (e.g. He, C, N, O, Al, Na, see reviews by Kraft 1994, Gratton et al. 2004, 2012, 2019). Chemical abundances of these elements follow distinctive patterns. The most studied ones include anticorrelations between Oxygen and Sodium, Carbon and Nitrogen, Magnesium and Aluminium (e.g. Carretta et al. 2009). The GCs host stars that resemble Galactic field stars together with stars enhanced in He, N, Al, Na and depleted C and O.

- **Horizontal branch second parameter** is the phenomenon of GCs with similar metallicities exhibiting different horizontal branch morphologies (e.g. Catelan 2009, Dotter et al. 2010, Milone et al. 2014, Tailo et al. 2020 and references therein).

- **Multiple sequences in the photometric diagrams** More recently, it has been discovered that the distribution of GC stars in the color-magnitude diagram (CMD) is not consistent with a single isochrone. Multiple or broad sequences have been observed across the whole color-magnitude diagram (main sequence, sub-giant branch, red giant branch, white dwarf cooling sequence). These sequences can be continuously traced on the CMD across all evolutionary phases of stars and are associated with stars with different chemical composition.

Nowadays it is widely accepted that most GCs host two main stellar populations. The first population, share the same chemical composition as Galactic field stars of similar metallicities, whereas second-population stars are enhanced in He, N, Al, Na and depleted in C, and O. The origin of first and second populations is still under debate. It is not firmly established whether or not first and second population stars originated in different star-formation episodes, for historical reasons they are referred to as first and second-generation stars (1G, 2G).

The discovery of multiple-populations from photometry of GCs, is mostly due to the Hubble Space Telescope (HST), which was able to clearly capture multiple sequences in color-magnitude diagrams (CMDs), and ground-based telescopes equipped with UV filters.

To identify the multiple populations, astronomers used various methods based on photometry. The main different photometric diagrams are summarized as follows:

- **Ultraviolet and optical photometry** is often used to disentangle stellar populations with different chemical compositions. Indeed, the stars with different He, C, N, O, Na abundances define different sequences in photometric diagrams that involve the U band like the the U vs U-B color-magnitude diagrams or the U vs $C_{U,B,I}$ pseudo CMD. The reason why the U$-$B color is an efficient tool to disentangle stars with different chemical composition is that the U filter includes NH and CN molecular bands, while B spans CH bands. Hence, the 2G stars, enriched in N and depleted in C, appear fainter in U and redder in U-B than the 1G stars with the same luminosity (e.g. Marino et al. 2008). Similarly F275W, F336W, F438W filters are widely used to study multiple populations with HST.

- **Wide color baseline** Stars with different He abundances but same luminosity exhibit different effective temperatures. Stars with pristine He content ($Y \sim 0.25$) are redder than He-rich stars due to their lower effective temperature. Hence, a wide color baseline allow us to disentangle MSs and RGBs composed of stars with different helium abundances. This phenomenon is illustrated in Figure 1 for NGC 2808 (Piotto et al., 2007).

- **Two-color diagrams** involving the combination of UV and optical filters are used to identify multiple populations. An example is the $m_{F275W} - m_{F336W}$ vs $m_{F336W} - m_{F438W}$ diagram is commonly used in studies of multiple populations with HST. In this diagram, the F275W and F336W filters include OH and NH molecular bands, while F438W spans CN and CH bands. Since 1G
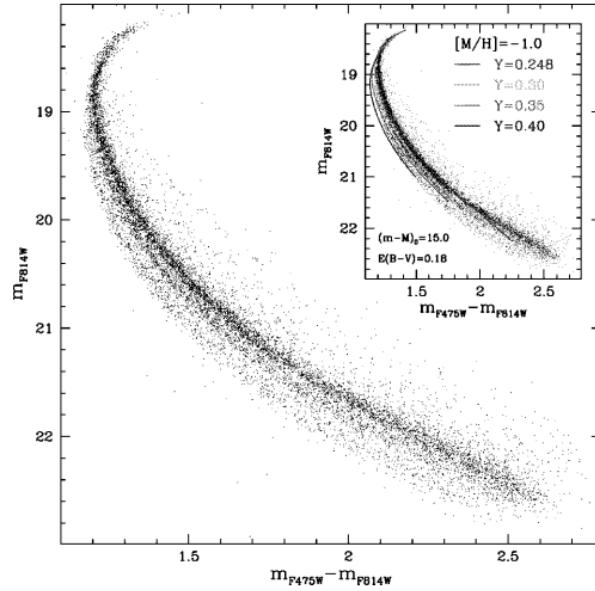
Figure 1: F475W-F814W vs F814W CMD of NGC 2808 by (Piotto et al., 2007). The inset compares the CMD and isochrones with various He contents.
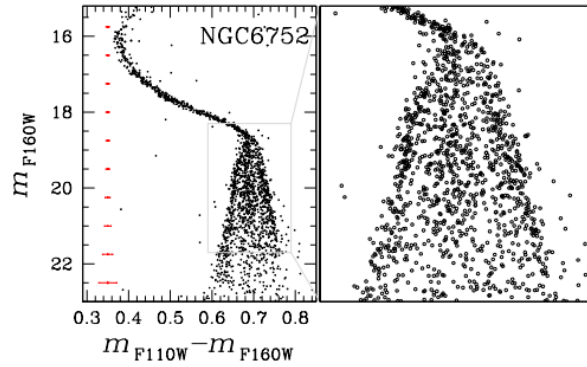
Figure 2: F110W-F160W vs F160W CMD by (Dondoglio et al., 2022). The panel on the right zooms in on the main sequence knee.

stars are rich in C and O, but are depleted in N, they are bright in F336W and faint in F275W and F438W.

- **Chromosome Map** The Chromosome map (ChM) is a pseudo two-color diagram of stars that belong to different sequences (MS, RGB, or AGB stars) derived from photometry in different filters that are sensitive to the specific chemical composition of GCs (Milone et al. 2015; Marino et al. 2017). It differs from a two-color diagram because the sequences of MS, RGB or AGB

stars are verticalized in both dimensions. The position of a star in the ChM is closely connected with its chemical composition. The 1G stars are clustered around the origin of fhe ChM, whereas 2G stars define an extended sequence. The fact that the distribution in the ChM of 1G and 2G sequences is wider than that expected from observational errors alone demonstrates that both 1G and 2G stars are composed of stellar sub-populations.

The F275W, F336W, F438W and F814W filters of HST are the most-widely used photometric bands to derive the ChM, but other optical and near-infrared filters of HST, including F606W, F814W, F110W and F160W are also excellent tools to build the ChM of M-dwarfs (Milone et al., 2017a).

- **Near-Infrared photometry** is used to detect multiple populations in M-type stars. Most of the studies are based on photometry derived from the F110W and F160W filters of HST. The F160W HST band is highly sensitive to oxygen-containing molecules including H_2O, while F110W is poorly affected by O. This means that 2G would have bright m_{F160W} and redder $m_{F110W} - m_{F160W}$ with respect to 1G. As an example, Figure 2 shows the F160W vs. F110W−F160W CMD of NGC 6752 (Milone et al., 2019; Dondoglio et al., 2021). The MS is narrow and well defined above the knee. Indeed, these MS stars are too hot for showing molecules in their atmospheres. On the contrary, three MSs are clearly visible below the MS knee (see Milone et al. 2019 for details).

The main observational properties of the multiple populations that have been inferred from both spectroscopy and photometry can be summarized as follows:

- **Specificity** 2G stars are commonly found in GCs but are extremely rare in the Milky Way field. This means that any formation scenario for the origin of multiple populations needs to take into account the special conditions in the early Universe that cause 2G stars to be born in the GC environment.

- **Ubiquity** The phenomenon of multiple populations is common to nearly all studied GC, meaning that multiple populations must be a direct consequence of GC formation.

- **Variety** While multiple populations are a common feature of GCs, in each GC it presents in a different manner. The number of multiple populations with different chemical compositions in a GC ranges from two (e.g. in M4) to 16 (in Omega Centauri). This means that the way in which 1G contributes to the formation of 2G varies from one cluster to another.

- **Predominance** 2G stars are a significant component in GCs. The fraction of 2G stars ranges from more about 40% in small mass GCs to more than 90% in Omega Centauri and correlates with cluster mass (Milone et al. 2017, 2020).

- **Discreteness** Most GCs show discrete sequences of 1G and 2G in the CMDs and distinct conglomerates of stars in the ChMs.

4

- **Supernova avoidance** 1G and 2G stars tend to share the same metallicity with extreme exceptions like Omega Centauri and Terzan 5. Even in such extreme cases, only 2% of iron ejected from 1G core-collapse supernovae needs to be retained to enrich 2G stars in Omega Centauri to the observed [Fe/H] ratio. This means that even for a current fraction of 1G stars (which was likely higher at formation), the core-collapse supernovae would produce $10^3 M_\odot$ of iron, most of which would be ejected. Hence 2G stars exhibit minimal contamination by supernova ejecta, meaning that any formation scenario should account for avoidance of supernova ejecta.

- **2G chemical abundances** 2G stars have chemical abundances from CNO cycle and p-capture processes. This means that in formation scenarios, 1G stars should be able to produce such elements. However, this ability of 1G donors is highly dependent on stellar models used. This property can disprove both the validity of the stellar model and of the formation scenario.

- **Helium Enrichment** 2G stars exhibit enrichment in He across most GCs.

- **Dependence on cluster mass** The fraction of 1G stars anti-correlates with cluster mass. This means that while in small mass GCs there is almost a 1:1 ratio between 1G and 2G stars, large mass GCs are dominated by 2G stars. In addition, there is evidence that N and He variation increases with cluster mass (Milone et al. 2017, 2020).

- **Dependence on initial mass** According to simulations, the fraction of 1G stars depends on initial mass. Small initial mass clusters do not host multiple populations, while the bigger ones do. The minimum mass to host multiple populations is $10^5 M_\odot$. This means that complexity of multiple populations increases with initial mass of the host cluster.

- **Dependence on GC orbit** GCs with large perigalactic radius $R > 3.5 kpc$ host a larger number of 1G stars. GCs with lower mass were more massive at formation, losing most of its 1G stars. Consequently GCs with a larger radial distance from the center should have a larger fraction of 1G stars due to gravitational influence of the host galaxy. Thus, interactions with the host galaxy impact the number of 1G and 2G stars.

- **Anisotropic motions** 2G stars exhibit anisotropic motions in more massive GCs. However both 1G and 2G of less massive GCs exhibit isotropic distribution of velocity.

1.2 Formation Scenarios

The main scenarios for the formation of multiple populations can be summarized into two main different categories.

Some formation scenarios, hereafter multi-generation scenarios, suppose that these stellar populations formed in multiple bursts of star formation. In this case, 1G stars form from pristine material, while 2G originate from a distinct star-formation episode from the gas, polluted by 1G evolution cycle.

These scenarios pose a significant implication, commonly referred to as Mass-Budget phenomenon. 2G stars represent the majority of stars in GCs. There is currently a small number of 1G stars that can produce the amount of gas, required to form 2G. This leads us to hypothesize that GCs were much more massive at formation (by a factor of 5-20) and later lost $80-90\%$ of their mass. These ancient GCs must have significantly contributed to the cosmic reionization and assembly of galactic halo (e.g. Renzini 2017).

However, another family of formation scenarios are based on the idea that multiple populations form in a single burst of star formation, making all stars in the GC coeval. According to this theory, all GC stars are coeval and the chemical composition that we observe in the so-called 2G stars is the product of accretion onto already formed stars of polluted material material from more massive stars of the same generation.

Milone & Marino 2022 and Renzini et al. 2016 discuss the formation scenarios for multiple populations in GCs in great length, which I summarize here.

1.2.1 Multi-generation scenarios

Supermassive stars According to Denissenkov & Hartwick 2013, the most massive stars migrate to the center of the GC due to dynamical friction and form a supermassive star (SMS) of $10^3 M_\odot$. This star is fully convective, making this object chemically homogeneous. The luminosity is either reaching or above the Eddington limit, that defines the maximum luminosity a stellar object can have while staying in equilibrium. Due to radiation pressure the SMS would lose mass at a high rate and, in the process of evolution, the wind would get enriched in p-capture reactions, CNO cycle residuals and He. These conditions form a perfect environment to cradle 2G stars.

Fast rotating massive stars In this scenario Krause et al. 2013 describes the fast rotating massive stars (FRMS) that rotate near the break-up limit. Hot Hydrogen burns in the core of such stars. Due to rotation, the polluted material from the core is brought up to the surface. Equatorial winds cause FRMS to lose their mass to the surrounding disc, where 2G forms from ashes of FRMS and products of 1G evolution. However, in this scenario we would expect a continuous chemical distribution in stellar populations. Moreover, this process cannot be specific to GCs, so we should also observe 2G stars in the Milky Way field, which is hardly the case.

Massive interacting binaries Massive interacting binaries (MIB) are first introduced by de Mink et al. 2009 and then improved by Bastian et al. 2013. These authors consider binary systems consisting of $15 M_\odot$ and $20 M_\odot$ stars. Gravitational interactions between binaries shed almost $10 M_\odot$ of material from the envelope of the primary star. Due to small velocity of ejecta it is retained by the GC and, mixed with pristine gas, forms 2G stars.

Asymptotic Giant Branch stars This scenario is based on intermediate-mass stars in GCs during their asymptotic giant branch (AGB) evolution. They experience a hot-bottom burning process: the base of the surface convective envelope is hot enough to allow for nuclear burning, resulting in efficient p-capture nuclear processes.

In this formation scenario, 1G forms in the GC in a single starburst episode. All remaining gas is ejected by a supernova explosion, losing all Fe-enhanced material. 1G stars enter the AGB era and develop low-velocity ejecta of approximately 10 km/s. These winds are retained in the potential well of the GC and pollute the gas. 2G stars form in a separate starburst episode at small radial distance from the center, from pristine gas mixed with AGB ejecta. 1G stars are lost due to interactions with the parent galaxy since they formed in the outskirts of the GC while 2G stars are retained because they are centrally concentrated.

AGB stars must have masses ranging from $3M_\odot$ to $8M_\odot$, where the lower limit is the minimum mass required to produce a carbon star.

Multiple stellar populations as a case of cooling Scenario by Renzini et al. 2022 proposes that GCs form before the assembly of the main body of the Milky Way, inside pre-galactic dwarfs. A rarer case of similar conditions occurred during the galactic bulge formation in metal rich GCs.

In this scenario, authors theorize that the most massive stars sink into black holes and in particular that stars of $20-40M_\odot$ do not explode as supernovae. This inhibits star formation feedback right after the formation of 1G.

Runaway stellar formation is the major implication of feedback suppression. Residual gas combined with the binary star ejecta forms stars up to the supernova stage. CNO-cycle and p-capture materials are ejected by 1G binaries during the common envelope phase, forming 2G stars. In the absence of feedback, over-cooling would turn all the baryons into stars in the Early Universe.

1.2.2   Accretion Scenarios

Supermassive stars Gieles et al. 2018 suggest a scenario where super-massive stars are responsible for the chemical composition of 2G stars. Following the idea by Denissenkov & Hartwick (2014), they suggest that due to gas accretion the proto-GC undergoes an adiabatic contraction and dramatically increases the star-collision rate. When the cluster reaches high density, this phenomenon leads to the formation of a super-massive star (SMS) via runaway collisions. Gieles et al. 2018 suggest that GCs experience one star formation episode only, but some of the 1G stars are polluted by the ejecta of the SMS star. Specifically, the polluted material released by the SMS winds is then diluted with pristine gas and accreted onto the protostars, thus forming 2G stars.

Early disc accretion In this scenario (Bastian et al., 2013) combines FRMS and MIB, theorizing all stars within GCs to form in a single burst of star formation. Material, polluted by FRMS and MIB is accreted in the disc of protostars. This material matches the unusual abundances of GCs and solves the Mass Budget Problem.

1.3   Multiple populations in 47 Tucanae

In this thesis, I investigate the Globular Cluster NGC 0104, commonly known as 47 Tucanae. 47 Tucanae is a typical metal-rich GC and is affected by low interstellar extinction (Carretta et al., 2004). It is a part of the Toucan constellation in the Southern sky and lies 13,000 light years away. It can be observed with a naked

eye ($m \sim 4.1$) next to the Small Magellanic Cloud. It is one of the most massive, dense and luminous GCs in the Milky Way (e.g. Baumgardth & Hilker 2018). It is relatively close to Earth and is located at high Galactic Latitude, so it was widely observed by main space-based telescopes, including HST, CHANDRA, SPITZER, and JWST (Ye et al., 2022; Milone et al., 2023). It is also widely studied in the context of multiple populations. Early photometric evidence that 47 Tucanae is not consistent with a simple stellar population is provided by the detection of a color spread in the MS of 47 Tucanae and a multimodal SGB, which was attributed to He variations of 0.02-0.03 (Criscienzo et al., 2010; Nataf et al., 2011). Nowadays multiple sequences are detected along the main evolutionary phases of 47 Tucanae as illustrated in Figure 3.
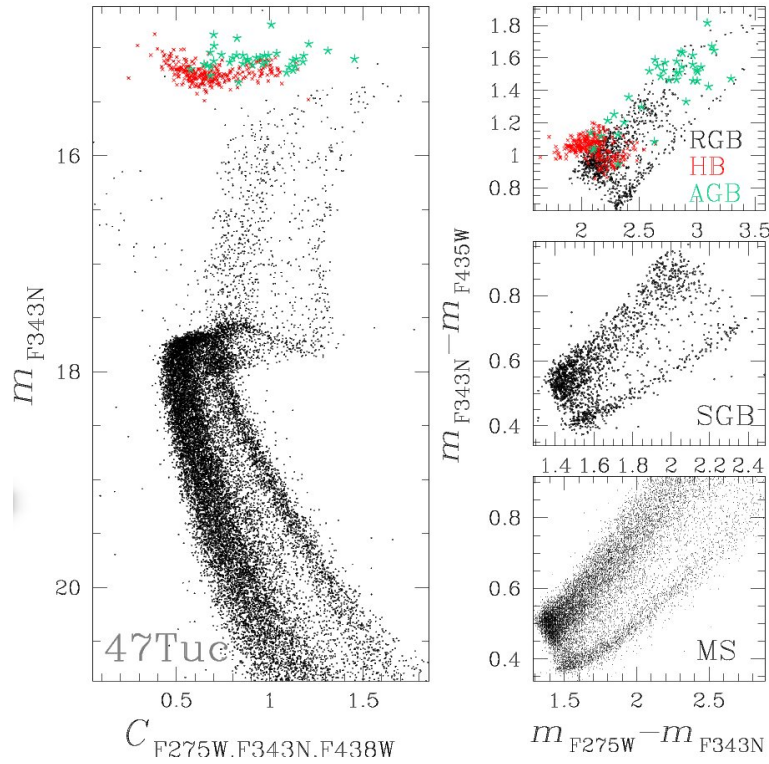
Figure 3: Photometric diagrams derived from UVIS/WFC3 F275W, F336W and F438W filters *Left panel.* $F343N$ vs. $C_{F275W,F343N,F438W}$ (Milone et al., 2013). *Right panel.* F343N-F438W vs. F275W-F343N of 47 Tucanae from Milone et al. 2012 *Top.* Red giant branch, horizontal branch, asymptotic giant branch *Middle.* Subgiant branch *Bottom.* Main sequence stars

Studies based on spectroscopy reveal that 47 Tucanae exhibit the classical C-N, O-Na anticorrelations and that its stars span a range of [O/Fe] of about 0.6 dex (e.g. Carretta et al. 2009, Cordero et al. 2014, Marino et al. 2016).

In this chapter I have introduced the notion of multiple populations and discussed detection methods. I have summarized the main properties of multiple

populations that need to be taken into account by formation scenarios. I have discussed existing work in 47 Tucanae GC, drawing comparisons between the low- and high-mass stars and their chemical abundances.

This thesis is organized as follows: Chapter 2 characterizes the photometric data set and the procedure of data reduction; Chapter 3 introduces the methodology of deriving the color-magnitude diagrams and chromosome maps; Chapter 4 illustrates the results; Chapter 5 discusses the implications in characterizing the origin of multiple populations among VLM stars.

2 Data Reduction

In this Chapter, I describe the data set used in this thesis and the methods of obtaining the photometry and astrometry of stars in the direction of 47 Tucanae. Moreover, I discuss the procedure of star selection with high-precision determinations of magnitudes and positions.

2.1 Data

To investigate the multiple stellar populations of 47 Tucanae I used data collected by the Hubble Space Telescope (HST). It is a space-based telescope launched in 1990 which revolutionized the field of astronomical observations. The observational capabilities of the telescope span a wide wavelength interval that ranges from the ultraviolet to near-infrared. It orbits just above the Earth atmosphere at speed of 17,000 miles per hour, completing every orbit in approximately 55 minuts.

HST has two primary cameras for imaging, namely the Advanced Camera for Surveys (ACS) and the Wide Field Camera 3 (WFC3). The latter is sensitive to a wavelength range that goes from the Ultraviolet through visible light and into the near-infrared (NIR).

WFC3 is implemented with a dual-channel design. The incoming light is directed into the camera with a pick-off mirror and is then directed to either the Ultraviolet-Visible (UVIS) channel or the infrared channel (IR). The detectors in both channels are solid-state devices.

For this work, I used images collected through the F390W and F160W bands of UVIS/WFC3, whose main properties can be summarized as follows:

- **F606W** $\lambda_{min} = 4712.79\mathring{A}$; $\lambda_{max} = 7208.10\mathring{A}$; Effective width of $2038.40\mathring{A}$; $FWHM = 2295.32\mathring{A}$

- **F390W** $\lambda_{min} = 3259.29\mathring{A}$ $\lambda_{max} = 4470.97\mathring{A}$; Effective width of $814.06\mathring{A}$; $FWHM = 907.27\mathring{A}$.

The IR/WFC3 filters used in this work include:

- **F110W** $\lambda_{min} = 8845.79\mathring{A}$; $\lambda_{max} = 14122.58\mathring{A}$; Effective width of $3856.85\mathring{A}$; $FWHM = 4637.84\mathring{A}$.

- **F160W** $\lambda_{min} = 13857.70\mathring{A}$ $\lambda_{max} = 17003.09\mathring{A}$; Effective width of $2750.15\mathring{A}$; $FWHM = 2876.73\mathring{A}$.

All the images are retrieved from The Mikulski Archive for Space Telescopes (MAST), which is a NASA-funded project, aimed at archiving astronomical data.

In this thesis, I am analysing two sectors with different radial separations from the center of 47 Tucanae. From now these sectors will be referred to as Sector A and Sector B, and their footprints are provided in Figure 4.

Sector A is located at $RA{\sim}00^h22^m35^s, DEC{\sim}{-}72^d10^m00.4^s$, $\sim$410 arcsec from the cluster center. Sector B is located at $RA{\sim}00^h21^m23^s, DEC{\sim}{-}72^d02^m36^s$, about 680 arcsec from the center.

The main properties of all the images, including the ID, filter, date of observation, coordinates and exposure time are listed in Table 1 and 2 for the Sector A and B, respectively.
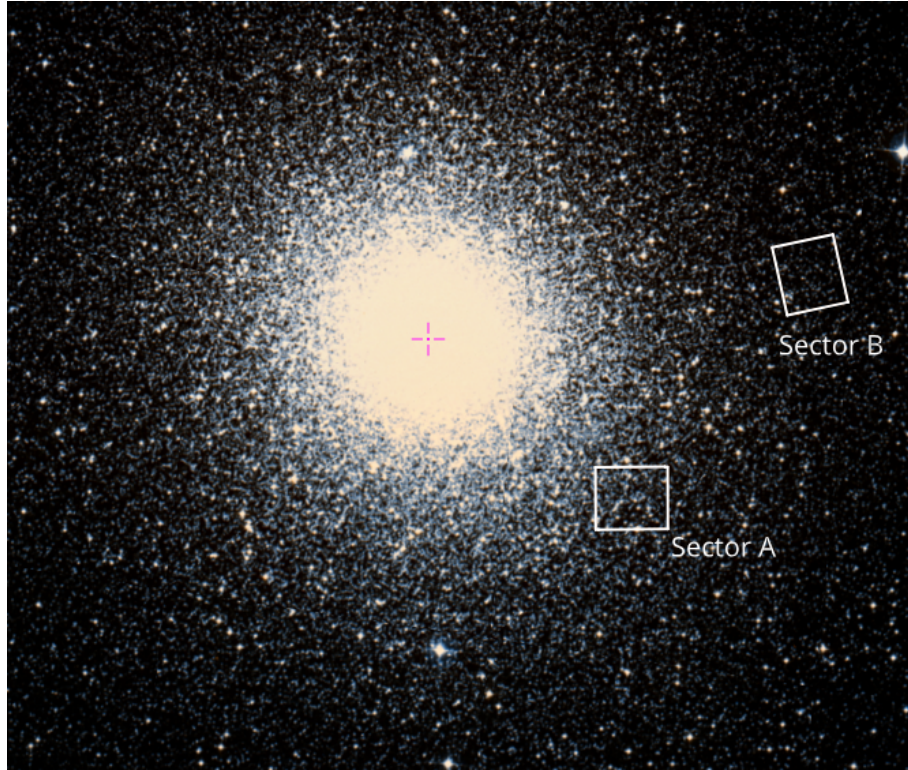
Figure 4: Image of 47 Tucanae from ground-based telescopes, obtained from MAST. I provide the footprints of Sectors A and B.

2.2 Data Reduction

To measure the magnitudes and fluxes of the stars in each image I used the procedure and computer programs developed by Jay Anderson and his collaborators (e.g. Anderson & King, 2000; Anderson et al., 2008; Sabbi et al., 2016). I first analyze each exposure separately and then average the determinations of the coordinates and fluxes of each stars derived in various exposures to obtain the best estimates of its position and magnitude.

2.2.1 Photometry and astrometry of stars in individual images.

The data reduction for UVIS/WFC3 images is carried out with the FORTRAN computer programs developed by J. Anderson. The method by Anderson and collaborators is based on the empirical point-spread-function (PSF) model. I first derived the stellar positions and fluxes in each exposure, separately, and then averaged the results from the various exposures to derive the best determinations of coordinates and magnitudes.

The PSF describes the response of the telescope to a point-like source. Since GCs are located at large distances from the Sun, their stars are point-like sources

Table 1: Images collected with the WFC3 camera for the sector A.

Image ID	Filter	Date	RA	DEC	Exposure time (s)
ib6v01e1q			00d22m35s8	−72:10:00.4	1399
ib6v01e4q	F110W	13/02/10	00d22m35s8	−72:10:00.4	174
ib6v01e6q			00d22m37s0	−72:10:00.3	1399
ib6v01e9q			00d22m37s0	−72:10:00.3	102
ib6v01ebq			00d22m35s8	−72:10:00.4	1199
ib6v01eeq			00d22m35s8	−72:10:00.4	299
ib6v01egq			00d22m37s0	−72:10:00.3	1199
ib6v01ejq	F160W	13/02/10	00d22m37s0	−72:10:00.3	299
ib6v01elq			00d22m34s7	−72:10:00.6	1199
ib6v01eoq			00d22m34s7	−72:10:00.6	299
ib6v01eqq			00d22m34s7	−72:10:00.6	1199
ib6v01etq			00d22m34s7	−72:10:00.6	299
ib6v01dgq			00d22m34s4	−72:09:58.7	50
ib6v01dhq	F390W	13/02/10	00d22m34s4	−72:09:58.7	1355
ib6v01dlq			00d22m35s6	−72:09:58.6	1206
ib6v01doq			00d22m35s6	−72:09:58.6	50
ib6v01drq			00d22m34s4	−72:09:58.7	50
ib6v01dtq	F606W	13/02/10	00d22m34s4	−72:09:58.7	1347
ib6v01dvq			00d22m35s6	−72:09:58.6	1402
ib6v01dyq			00d22m35s6	−72:09:58.6	50

and are described by a PSF. In a CCD image, the PSF determines the amount of stellar flux that falls in a pixel located at a given position with respect to the star's center. A point source is defined by three main parameters: positions and total flux (X, Y, Z). The main task of astrometry and photometry is to derive these parameters from the image as accurately as possible.

The PSF can be described as function $\phi(\Delta X, \Delta Y)$ that allows me to determine the fraction of a star's flux that I expect in a pixel located at a given offset $(\Delta X, \Delta Y)$ from the star's center. At odds with other programs for the determination of the PSF (e.g. DAOPHOT, Stetson 1987), the PSF model that I construct is not based on an analytical function, but it is represented by an empirical grid of points that are derived from a sample of observed stars.

This method is based on the fact that each star in the image is represented by an array of pixels P(i, j) that can be fitted by the PSF model to derive the three parameters: X, Y, Z. The sky (s) is derived from an annulus of pixels that surround the star.

Similarly, if we have the positions and fluxes for a star we can turn out the relation above and solve for the PSF:

$$\phi(\Delta X, \Delta Y) = (P_{i,j} - s)/Z \qquad (1)$$

As a consequence, each pixel in the star's image provides information on the PSF function at one point that is located at $(\Delta X, \Delta Y) = $ (i-X, j-Y). I can thus

Table 2: Images collected with the WFC3 camera for the sector B,

Image ID	Filter	Date	RA	DEC	Exposure time (s)
ib6v06caq			00d21m23s8	−72:02:36.5	1399
ib6v06cdq	F110W	12/06/10	00d21m23s8	−72:02:36.5	174
ib6v06cfq			00d21m23s6	−72:02:41.8	1399
ib6v06cjq			00d21m23s8	−72:02:36.5	1199
ib6v06cmq			00d21m23s8	−72:02:36.5	299
ib6v06coq			00d21m23s6	−72:02:41.8	1199
ib6v06crq	F160W	12/06/10	00d21m23s6	−72:02:41.8	149
ib6v06ctq			00d21m24s0	−72:02:31.3	1199
ib6v06cwq			00d21m24s0	−72:02:31.3	299
ib6v06cyq			00d21m24s0	−72:02:31.3	1199
ib6v06d1q			00d21m24s0	−72:02:31.3	149
ib6v06c0q			00d21m24s4	−72:02:30.6	50
ib6v06c2q	F606W	12/06/10	00d21m24s4	−72:02:30.6	1347
ib6v06c4q			00d21m24s2	−72:02:35.8	1252
ib6v06c7q			00d21m24s2	−72:02:35.8	50
ib6v06bpq			00d21m24s4	−72:02:30.6	50
ib6v06bqq	F390W	12/06/10	00d21m24s4	−72:02:30.6	1400
ib6v06buq			00d21m24s2	−72:02:35.8	1048
ib6v06bxq			00d21m24s2	−72:02:35.8	50

construct a PSF model by combining the array of samplings from a large sample of stars.

To do that, I need an iterative procedure. Indeed, it is not possible to derive accurate values of X, Y, and Z without an accurate PSF model. Similarly, without good positions and fluxes, I cannot derive an accurate PSF.

To derive the PSF models I used the computer program *img2psf* and the iterative procedure introduced by Anderson & King 2000.

At the first iteration I used an archive PSF to identify a sample of isolated, bright, and not-saturated stars and estimate a first guess of their magnitudes and positions. These stars are then used to construct an improved PSF model and the procedure is iterated, until two subsequent PSF models exhibit negligible differences only. To do this I used the following arguments as inputs for the *img2psf* program.

- **HMIN: 13** defines the isolation index, the minimum distance for two stars to be considered isolated. This distance is defined in pixels, from the brightest pixel of one star to another.

- **FMIN: 3000** defines the minimum flux for the brightest pixel of a star to be included in the calculation.

- **PMAX: 54000** defines the maximum flux for the central pixel of a star to be included in the calculation. The adopted value allows us to use unsaturated

stars alone in the determination of the PSF.

- **QMAX: 0.3** defines the maximum value of the quality-fit parameter, which is a parameter derived from the comparison between the PSF model and the observed source. The Q-fit is indicative of the quality of the PSF, with Q-fit=0 corresponding to the ideal PSF model. The adopted value of QMAX allows to exclude cosmic rays, galaxies and blended stars.

- **NSIDEs: 2** defines the number of regions the image is divided into to calculate the perturbation of the PSFs. In this case I divided each UVIS/WFC3 chip into 2×2 regions. This choice is the result of a compromise. On one hand I need wide enough regions (i.e. a large area) to maximize the number of stars used to calculate the PSF. On the other hand I need regions with a small area to constrain the small-scale nonlinear variations of the PSF.

The program iterates and improves both the PSF model and the stellar positions and fluxes until the PSF converges. In the end it produces a grid of 7×4 PSFs in each CCD, as shown in Figure 5. Since the PSF shape depends on the physical position on the CCD due to charge diffusion and optical aberrations, I accounted for spatial variations across the field of view. PSF is then interpolated over the neighbouring grid points to fit any point on the CCD.

Figure 5: An example of an 8×7 grid of PSFs

To measure the coordinates and the magnitude of each star I used the *img2xym* program, which employs the PSF models derived above to calculate for stellar positions and fluxes. Specifically, I derived for each exposure:

- the coordinates X and Y, in pixel units, in the reference frame of the UVIS/WFC3 CCD

- the instrumental magnitudes, which are calculated as -2.5 times the logarithm of the total amount of digital numbers that define the image of a star in its central 5×5 pixel region.

I measured all the stars that are isolated within a radius of 5 pixels and limited the analysis to stars with a flux greater than 50 digital numbers in their brightest pixel.

Specifically, I used the following inputs:

- **HMIN: 5** The isolation index and defines the minimum distance between two stars to be measured as isolated.

- **FMIN: 50** The minimum flux for the brightest pixel of the star

- **PMAX: 10e9** The maximum flux for the central pixel of a star to be included in the catalogue.

In order to derive the PSF I used only bright isolated sources. I also derive photometry for faint and saturated stars. The choice of 50 is a compromise to measure faint stars in a reasonable amount of computer time. At this stage stellar magnitudes and positions are measured in each image separately.

To measure the magnitudes and positions of stars in the IR images I adopted a procedure similar to that described above for the UVIS/WFC3 exposures.

In this case, I used the *hst1pass* computer program (Anderson, 2022), which both derives the best PSF model suitable for each image and calculates the photometry and astrometry for all sources.

For saturated UVIS/WFC3 stars the photometry was performed using the method developed by Gilliland (2004), which recovers the electrons that have bled into neighbouring pixels. We refer to Section 8.1 in Anderson et al. 2008 for details on the application of this method.

2.2.2 Selection of stars with high quality photometry

The computer program *img2xym* computes the quality-fit parameter for each stars (q-fit, Anderson et al. 2008) which provides information about the fit between the PSF model and the observed star.

As an example, Figure 6 shows the q-fit parameter derived for stars observed in the F606W band as a function of the instrumental magnitude. The perfect match between the PSF and the star would correspond to a q-fit equal to zero, whereas large q-fit values indicate a poor fit. Most of the sources in Figure 6 follow a clear trend. The bulk of bright and non-saturated stars, with magnitudes fainter than $\sim$13.8 mag, have q-fit values smaller than 0.05 mag. The typical q-fit value for pointlike sources constantly increases towards fainter magnitudes and rises up to 1.0 at magnitude of ~ -6.0. However, for a fixed magnitude, we may notice a number of sources with larger q-fit values than those of the stellar objects. These high q-fit objects comprise galaxies, blended stars, cosmic rays, detector artifacts, whose profiles are very different from the PSF ones.

In this thesis, I used the q-fit parameter as a diagnostic to identify the probable non-stellar objects. To do this, I divided the magnitude interval between -14 and -5 mag in different bins of a fixed width of 0.5 mag. For each bin, I calculated the median of the q-fit values for all the stars in the bin and the corresponding root mean square (σ). I added four times σ to the the median value, associated the resulting quantity to the average magnitude of the stars in the bin, and linearly interpolated these points to derive the upper blue line of Figure 6. The latter separate the point-like objects (black points) from the sources with a profile that significantly deviates from the PSF shape. Only the stars below the blue line are included in the following analysis.
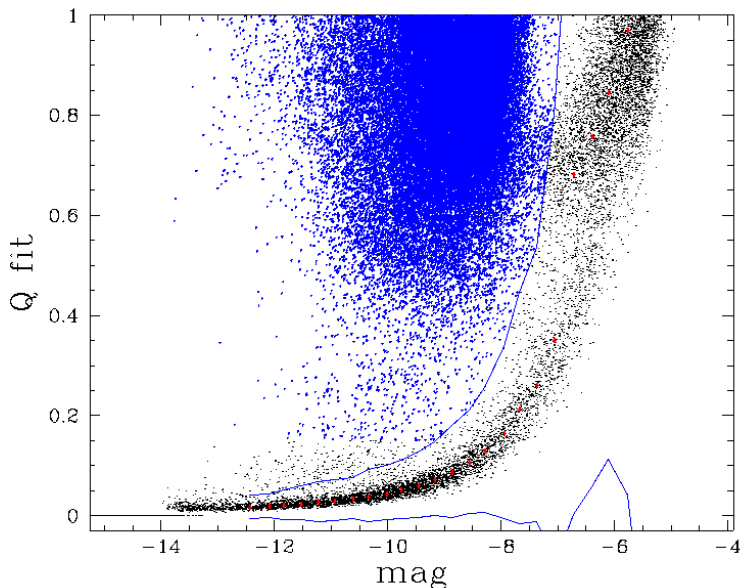
Figure 6: Quality fit parameter as a function of the instrumental F606W magnitudes for stars in Sector A. The sources above the blue lines are considered poorly measured ones and not included in the subsequent analysis. See the text for details.

Noticeably, the q-fit parameter is not calculated for saturated stars because they are not measured by means of PSF fitting. These stars are included in the following analysis but they do not affect the results of this thesis, which is focused on low-mass stars. This procedure was performed for all images in all filters in both sectors.

2.2.3   Photometry and astrometry of stars from multiple exposures

At this stage, the instrumental stellar magnitudes and positions I calculated from each image have different photometric and astrometric zero points that depend on various factors such as the exposure time or the position of the image in the plane of the sky.

17

To properly average the magnitude and position determinations derived from the different images I first transformed the coordinates and the fluxes of the stars of each image into a common reference frame. This procedure was performed from the images of each filter separately and resulted in four catalogs with the best determinations of X, Y, and magnitudes from the exposures in F390W, F606W, F110W, and F160W.

To do this, we first selected one image as a reference frame, and used the *xym2mat* program, which performs cross-identification between each image and the reference frame. It calculates matrices for each couple of images and searches for similar triangles where each vertex marks a star. These triangles are then rotated until giving a perfect match between the images.

The idea is based on the notion of *similar triangles*. A similarity transformation maintains congruent angles and ratios of corresponding sides. This allows the program to calculate two important quantities. If any triangle has three sides, namely long, intermediate and short:

1. Ratio of the intermediate side to the long one

2. Ratio of the short side to the long one

These quantities are the same for similar triangles and the program searches for this match in two images. Using least-square fitting the program identifies coefficients of the linear transformation: A, B, C, D, E, F. By employing these coefficients we are able to map coordinates of a star in one image (x_1, y_1) to another (x_2, y_2).

$$T(x_1, x_2) = (A + Cx_2 + Ey_2, B + Dx_2 + Fy_2)$$

Where T is the linear transformation used to convert positions of stars from each file into a common reference frame. Similarly I derive the constant to be added to the magnitudes of all stars in each image to transform them to the common reference frame provided by the master frame.

The input in this program is a text file, containing the following information, stored in rows. Below I report an example of such file for F606W filter, Sector A:

```
// IN.xym2mat
00 ib6v01dtq_WJCs.xym c8 f6 "m-13.7,-8.5"
01 ib6v01drq_WJCs.xym c8 f6 "m-13.7,-7.5"
02 ib6v01dtq_WJCs.xym c8 f6 "m-13.7,-8.5"
03 ib6v01dvq_WJCs.xym c8 f6 "m-13.7,-8.5"
04 ib6v01dyq_WJCs.xym c8 f6 "m-13.7,-7.5"
```

The first row defines the master frame, and corresponds to the images with the longest exposure time. The other lines refers to the available files, whose coordinates and positions will be transformed in the same reference frame as the master frame.

The columns provide important information:

- The first column is a running number.

- The second column lists the names of the files.

- The third and fourth columns define the camera and the filter used to obtain corresponding images. This information is crucial to correct the stellar positions for the effects of geometric distortion. Here I used the distortion solution by Bellini et al. (2013) for UVIS/WFC3 and Anderson (2022) for IR/WFC3.

- The fifth column provides the magnitude range of the stars used to compute the transformations.

The program includes an input parameter, specifying the radius around a star in the master frame within which the search for its counterpart in other frames is executed. For this thesis, I used 0.45 pixel.

As an example, in Figure 7 I plot the residuals in positions between the coordinates of the stars in the master frame and the coordinates of the stars derived from the ib6v01dvq image and transformed into the master system reference frame.
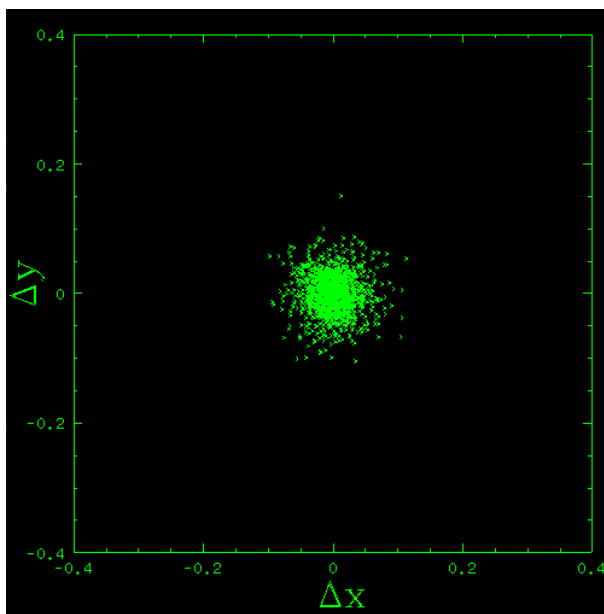
Figure 7: Position residuals between the F606W master frame of sector one and the ib6v01dvq image.

Finally, the *xym2bar* program first transforms the coordinates of each image into the master frame by using the six-parameter linear transformations computed by the *xym2mat* program, and then calculates the average coordinate. Similarly it computes the average magnitude of all stars after transforming the magnitudes of each image into a common master frame.

We imposed that each star must be measured in at least two images to be included in the final catalog.

The input file example is included below. Short exposure frames are used to obtain magnitudes for bright stars which are saturated in the long exposures. On the contrary, I derived the magnitudes and positions of the faint stars from the long exposures alone.

```
// IN.xym2bar
01 ib6v01drq_WJCs.xym c8 f6 "m-99,-10" # short exposure
02 ib6v01dtq_WJCs.xym c8 f6 "m-13.7,-4" # long exposure
03 ib6v01dvq_WJCs.xym c8 f6 "m-13.7,-4" # long exposure
04 ib6v01dyq_WJCs.xym c8 f6 "m-99,-10" # short exposure
```

The output file contains averages of positions and magnitudes of selected stars. The resulting catalogues:

- Sector 1: F606W, F390W, F110W, F160W

- Sector 2: F606W, F390W, F110W, F160W

The *xym1mat* program links two catalogues, specified by the user. The first input parameter is the master catalogue (F606W). The second input parameter is the reference catalogue.

Following a pattern similar to previous programs, the first iteration exclusively involved bright stars to reduce run-time. A successful match between two catalogues was achieved, along with a preliminary transformation between their respective reference frames. The second iteration introduces faint stars.

The output file contains all stars, common in two catalogues and magnitudes in both filters.

The resulting catalogues:

- F606W is used as a master catalogue

- F606W + F110W

- F606W + F160W

- F606W + F390W

2.3   Astrometric calibration

The coordinates of the stars in the catalogs derived in this thesis are transformed into a common reference system based on Gaia Data Release 3 (DR3) catalogues (Klioner et al., 2022), in such a way that the abscissa and the ordinate are aligned with the West and North direction, respectively.

To do this, I retrieved the catalog including 47 Tucanae stars in Sector A and B from Gaia DR3[1]. I first de-projected the right ascension and declination into the plane tangential to the center of each field, thus transforming the RA and DEC coordinates provided by Gaia DR3 into linear coordinates. Then, I identified the stars for which astrometry is available from both HST and Gaia DR3 and

---

[1]https://gea.esac.esa.int/archive/

used them to compute the six-parameter linear transformations that convert the coordinates from the reference frame of the HST catalog into the Gaia DR3 ones. To do this, I used the computer program *xym1mat*.

2.4 Photometric calibration

I calibrated the photometry of each filter and sector to the Vega mag system by calculating the aperture correction to the magnitudes derived by means of PSF-fit and applying to the corrected instrumental magnitude a photometric zero-point.

Specifically, I used the relation between the calibrated, m_{cal} and instrumental magnitudes, m_{inst}, from (Sirianni et al., 2005):

$$m_{cal} = m_{inst} + \Delta mag + ZP_{filter} + C \tag{2}$$

Where:

- Δmag is the aperture correction, i.e. difference between the PSF and the aperture photometry

- ZP_{filter} is the zero-point of our magnitude system in the WFC3 bands used in this thesis. We used the most-updated values of the zero points provided by the STScI webpage (Calamida et al., 2022).

- C is a constant that accounts for the amount of flux outside the 0.4 arcsec (or 0.5 arcsec for IR/WFC3 images) aperture. I used the tabulated encircled energy provided by the STScI website, to link the magnitudes to the infinite aperture for which we have calculated the zero-points.

The aperture photometry used to derive aperture corrections has been carried out with the computer program *drz_phot*.

In the case of the UVIS/WFC3 images I measured the aperture magnitudes within circular regions of 0.4 arcsec radius by using the drizzled and CTE-corrected (_drc) images, which are normalized to 1s exposure time. For the IR/WFC3 images which are not significantly affected by the CTE (Anderson & Bedin, 2010) I used the drizzled images (_drz) and a radius of 0.5 arcsec.

Input parameters are listed as follows:

- **HMIN: 10** Isolation index and defines the minimum distance in pixels between two stars to be considered isolated. As I derived the aperture correction exclusively using isolated stars, I chose a value of 10 pixels.

- **FMIN: 0.1** Minimum flux of the brightest pixel among the stars used for photometry derivation

- **PMAX: 10e9** Maximum flux of the brightest pixel among the stars used for photometry derivation. At this stage, I measured the aperture magnitude of saturated stars. Although they will not be included in the determination of the aperture correction, saturated stars are used to identify the stars for which both aperture and PSF photometry is available.

- **APPHOT:** "10.0 14.0 20.0" for UVIS/WFC3 and "4.01 7.0 10.0" for NIR/WFC3. The first numerical quantity defines the aperture radius used to derive the stellar magnitude, while the second and third values provide inner and outer radii of the annulus used to measure the sky level. All quantities above are in pixels.

To calculate for aperture corrections I used unsaturated and bright stars only with available aperture and PSF photometry. The procedure is illustrated in Figure 8 for the F606W images of Sector A. The PSF magnitude is displayed as a function of difference between the PSF and the magnitude aperture, Δmag.

The aperture correction was derived by means of an iterative procedure. At the first iteration, I use all the available unsaturated and bright stars (red symbols in Figure 8) to derive a first guess median value of Δmag and the corresponding dispersion σ. Then I reject stars with Δmag values that differ by more than $\pm 3\sigma$ from the median value and derive improved values of the median Δmag and σ. The procedure was iterated until two subsequent determinations of the median differ by less than 0.001 mag. The best estimate of the aperture correction is marked with a blue line in Figure 8, whereas the two vertical green lines are situated $\pm 3\sigma$ from the best estimate.
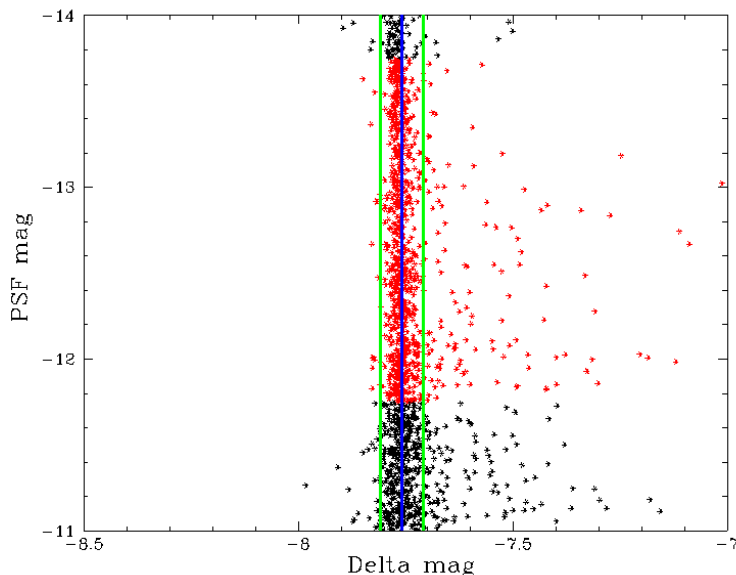
Figure 8: Instrumental magnitude derived from PSF fitting as a function of difference between the PSF magnitude and the aperture magnitude. Red symbols indicate the stars that have been used for the first-guess determination of the median Δmag value. The blue line marks the final value of Δmag, which is derived by using stars within the green lines. See the text for details.

47 Tucanae is located at large distances from the Galactic plane and is affected by low reddening (E(B−V)=0.04 mag, Harris 2010). Using the differential redden-

ing maps by Jang et al. 2022 I verified the analyzed field of view to be unaffected by a significant amount of differential reddening (smaller than E(B−V)=0.003 mag according to Legnardi et al. 2023). Hence I do not correct the photometry for the effect of differential reddening.

3 Data Analysis

In this chapter I present and analyse the photometric diagrams of 47 Tucanae, including the CMDs and the ChMs. In the subsequent analysis, unless specified, the same work has been performed on both Sector A and Sector B.

3.1 Color-Magnitude Diagram

To construct the CMDs, I first used the *xym1mat* computer program (Anderson & King, 2000) to identify the stars for which photometry in two or more filters is available. Specifically, I used six-parameter linear transformations to transform the coordinates of the stars in the reference frame of the F606W filter in the reference frame adopted for the other filters.

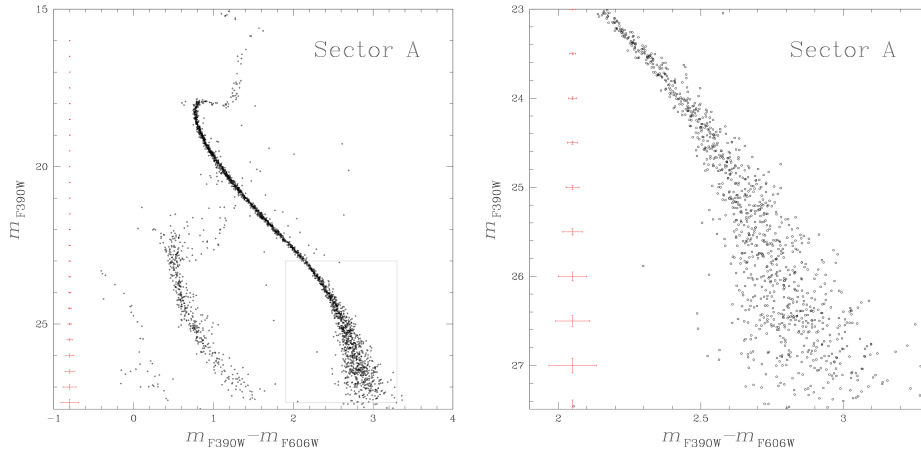The resulting CMDs are plotted in Figures 9–12 for stars in Sector A and B, separately.

Figure 9: *Left panel.* m_{F390W} vs. $m_{F390W} - m_{F606W}$ CMD for stars in Sector A. The gray box denotes the magnified region depicted in the next panel. *Right panel.* Zoom on the low MS. Photometric errors are shown in red in both panels.

The optical, m_{F390W} vs. $m_{F390W} - m_{F606W}$, CMDs (Figures 9 and 10) show the main evolutionary sequences of 47 Tucanae, including the red HB, RGB, SGB, MS, and the white-dwarf cooling sequence (WDCS). The latter corresponds to the sequence of stars with colors $m_{F390W} - m_{F606W} \sim 0$ mag. The right panel of Figures 9 and 10 are zoomed in on the bottom of the MS. Noticeably, the red HB, RGB, SGB, and MS of background Small Magellanic Cloud stars are visible between the WDCS and the MS of 47 Tucanae. As expected, Sector B hosts less 47 Tucanae stars in comparison to Sector A. Indeed it is situated in the outskirts of the GC.

Figures 13 and 14 illustrate the CMDs derived from optical and infrared photometry (m_{F110W} vs. $m_{F110W} - m_{F160W}$) for stars in sector A and B, respectively. The IR CMDs, m_{F110W} vs. $m_{F110W} - m_{F160W}$ are shown in the left panel of
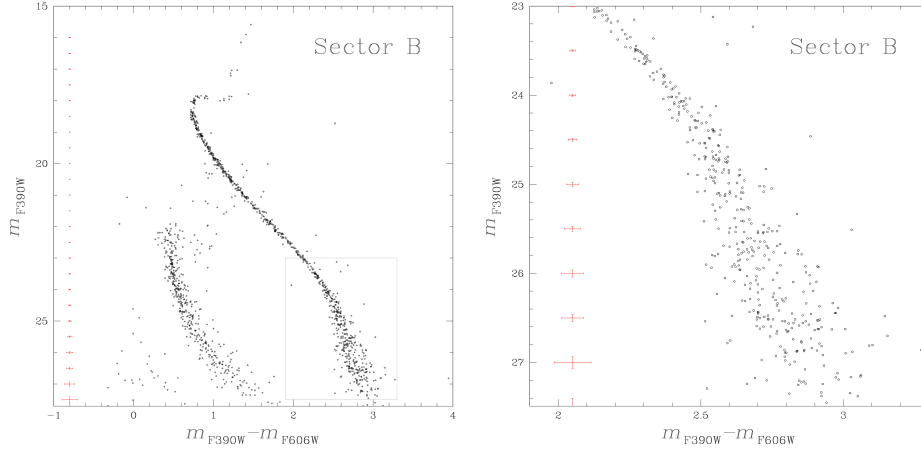
Figure 10: As in Figure 9 but for stars in Sector B.

Figure 11: *Left panel.* $m_{F606W} - m_{F110W}$ vs m_{F110W} CMD for Sector A. The gray box denotes the magnified region depicted in the next panel. *Right panel.* Zoom on the knee of $m_{F606W} - m_{F110W}$ vs m_{F110W} CMD of Sector A. Photometric errors are shown in red in both panels.

Figures 13 and 14, whereas the zooms of the same CMDs for faint MS stars of 47 Tucanae are provided in panels on the right.

In contrast with the CMDs composed of optical filters alone, the WDCS is not detectable in IR, while the evolutionary sequences of the SMC are clearly visible in the right panel of each Figure and mostly populate the bottom-left area of the CMD.

The CMDs of GCs can be powerful tools to identify and characterize multiple

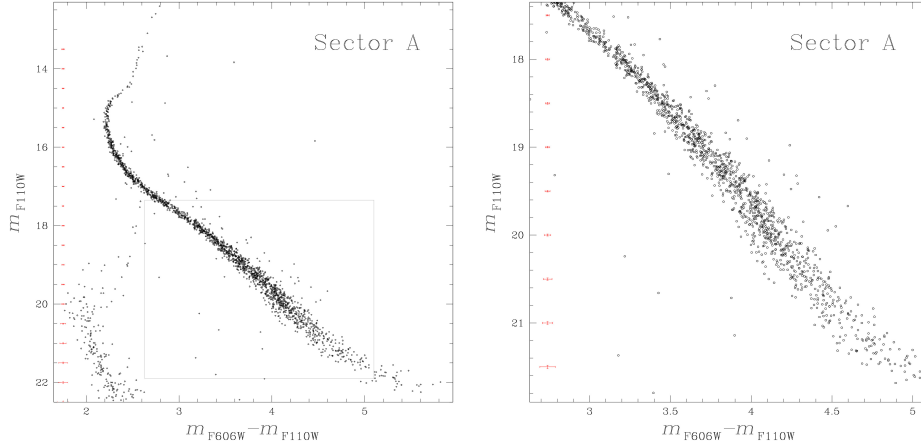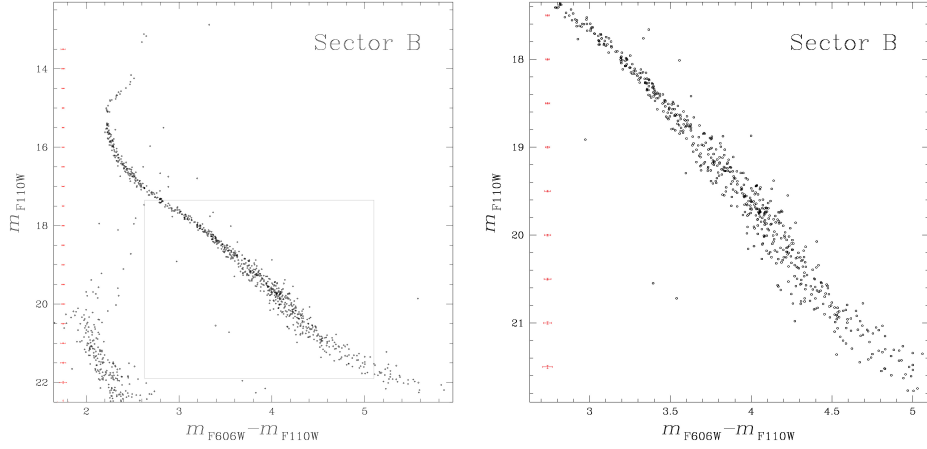Figure 12: Same as Figure 11 but for stars in Sector B.
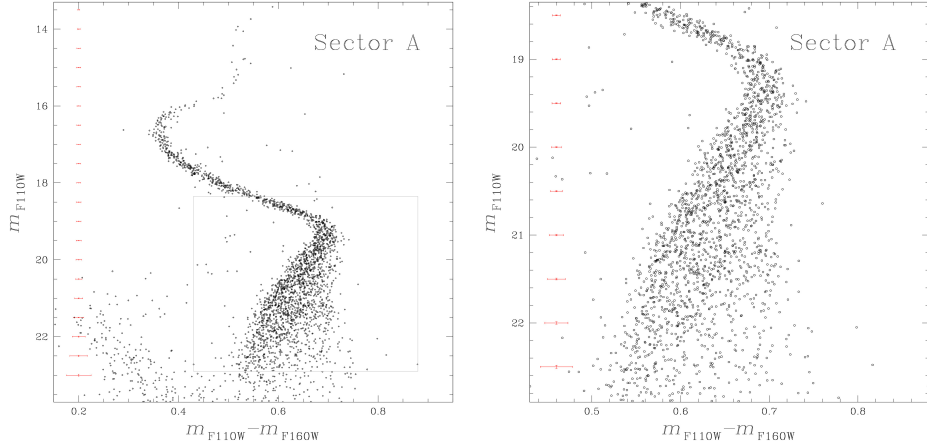
Figure 13: *Left panel.* $m_{F110W} - m_{F160W}$ vs m_{F110W} CMD for Sector A. The gray box denotes the magnified region depicted in the next panel. *Right panel.* Zoom on the knee of $m_{F110W} - m_{F160W}$ vs m_{F110W} CMD of Sector A. Photometric errors are shown in red in both panels.

stellar populations. In a simple stellar population, where all stars share the same age and chemical composition, a color spread among stars at the same evolutionary phase in the CMD is due to observational errors only. On the contrary, the evidence of a color broadening that is wider than that expected from the photometric errors indicates that the stars are not chemically homogeneous.

A remarkable feature of the IR CMDs is that while the SGB and the portion of the MS above the knee are narrow and well defined, the color spread of the

Figure 14: As in Figure 13 but for stars in Sector B.

M-dwarfs fainter than the knee significantly exceeds the color broadening due to photometric errors alone. A visual inspection of the CMDs suggest that the M-dwarfs with similar F110W magnitude exhibit a continuous color distribution.
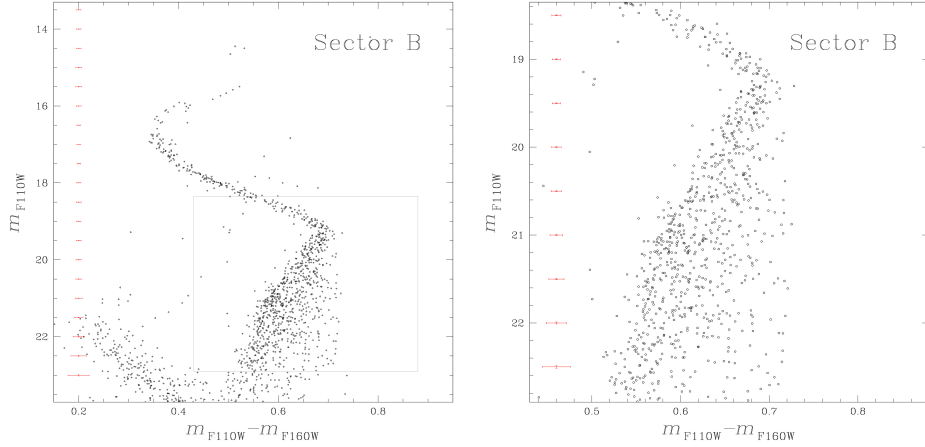
The majority of stars populate the blue portion of the MS, but I notice a tail of stars towards the red (see also Dondoglio et al., 2022; Milone et al., 2023, for details).

To better visualize the effect of observational errors on the MS broadening, I simulated a CMD that accounts for the photometric uncertainties. To do this, I first derived by hand the fiducial line of the MS, as illustrated in Figure 15, and simulate a sample of stars with the same luminosity function as the observed stars of 47 Tucanae and the same photometric errors.

The results are illustrated in the left panel of Figure 16, where the simulated stars (red symbols) are superimposed on the observed CMD. Moreover, I estimated the width of the observed MS at different F110W magnitude levels. To do this, I first verticalized the CMD by subtracting from the color of each star the color of the fiducial line with the same F110W magnitude. I divided the magnitude interval between $m_{\rm F110W} = 18.2$ and 23 mag into intervals of 0.25 mag and for each of them I estimated the difference, Δ, between 90th and the 10th percentiles of the color distribution in the verticalized diagram. I applied the same procedure to derive the values of Δ for the simulated CMD.

As shown in the right panel of Figure 16, the values of Δ of the observed stars (black starred symbols) are comparable with those of simulated stars (red circles) above the MS knee. Below the knee the color broadening of the observed MS is much wider than that expected by photometric uncertainties alone, thus corroborating the evidence that the M-dwarfs of 47 Tucanae host multiple stellar populations.

28
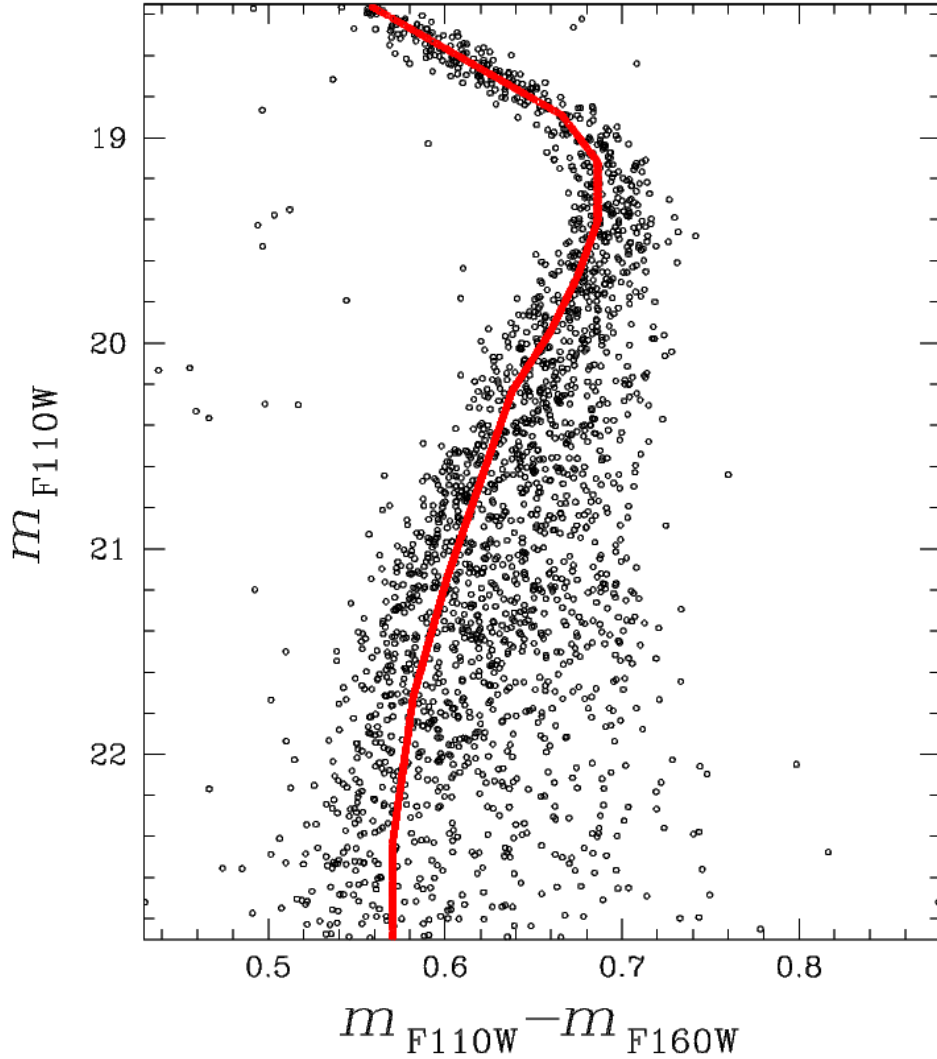
Figure 15: Reproduction of the CMD of 13. The fiducial line superimposed on the CMD is colored red. See the text for details.

3.2 Comparison with the isochrones

To better understand the physical reason that is responsible for the broadening of the low-MS of 47 Tucanae, I compared the observed IR CMD with isochrones from the Dartmouth database (Dotter et al., 2008), which account for the light-element abundance of the multiple populations as in (Milone et al., 2023). All isochrones share the same age of 12 Gyr, reddening E(B−V)=0.01 mag and distance modulus $(m − M)_0$=13.21 mag that provide the best fit with the upper MS and the SGB. These values are comparable with similar quantities derived from the literature

Figure 16: *Left panel.* Black points reproduce the CMD of Figure 13, whereas the simulated stars are colored red. *Right panel.* Difference of the 90th and 10th percentile of observed 47 Tucanae stars (black) and simulated stars (red).

(Dotter et al. 2010, Harris 2010, Tailo et al. 2020).

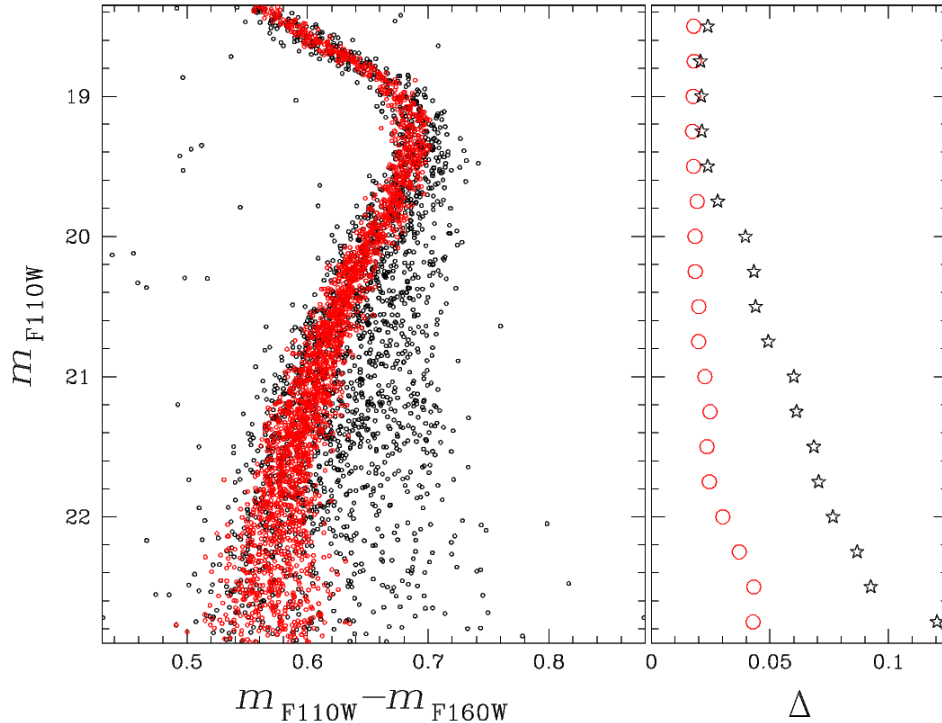As widely discussed in the literature, isochrones with different helium content are responsible for a split of the MS region above the knee (Piotto et al., 2007; Ziliotto et al., 2023; Norris, 2004) but nearly overlap in the F110W−F160W colors in the MS segment below the knee. On the contrary, isochrones with different oxygen abundances overlap with each other above the MS knee, where the stars are too hot to exhibit molecules in their atmospheres, but exhibit different colors among M-dwarf stars with similar luminosity, due to various molecules (e.g. TiO, VO, and H_2O), which mostly affect the region of the spectrum of the F160W band.

By comparing the observed MS width in the F110W−F160W color, with isochrones with different oxygen abundances (aqua and red isochrones of Figure 17, I find that an internal [O/Fe] difference of 0.6 dex is needed to reproduce the observed CMD and ChM (Milone et al., 2023). Such oxygen variation is similar to that observed among RGB stars by means of high-resolution spectroscopy (Carretta et al., 2009; Marino et al., 2016). I conclude that RGB stars with masses of about 0.8 $M_\odot$ and M-dwarfs with masses of $\sim 0.2 - 0.4 M_\odot$ share the same oxygen abundances.

The determination of the amount of oxygen variations among stars of different masses helps us to constrain the formation scenarios. In scenarios where the 1G
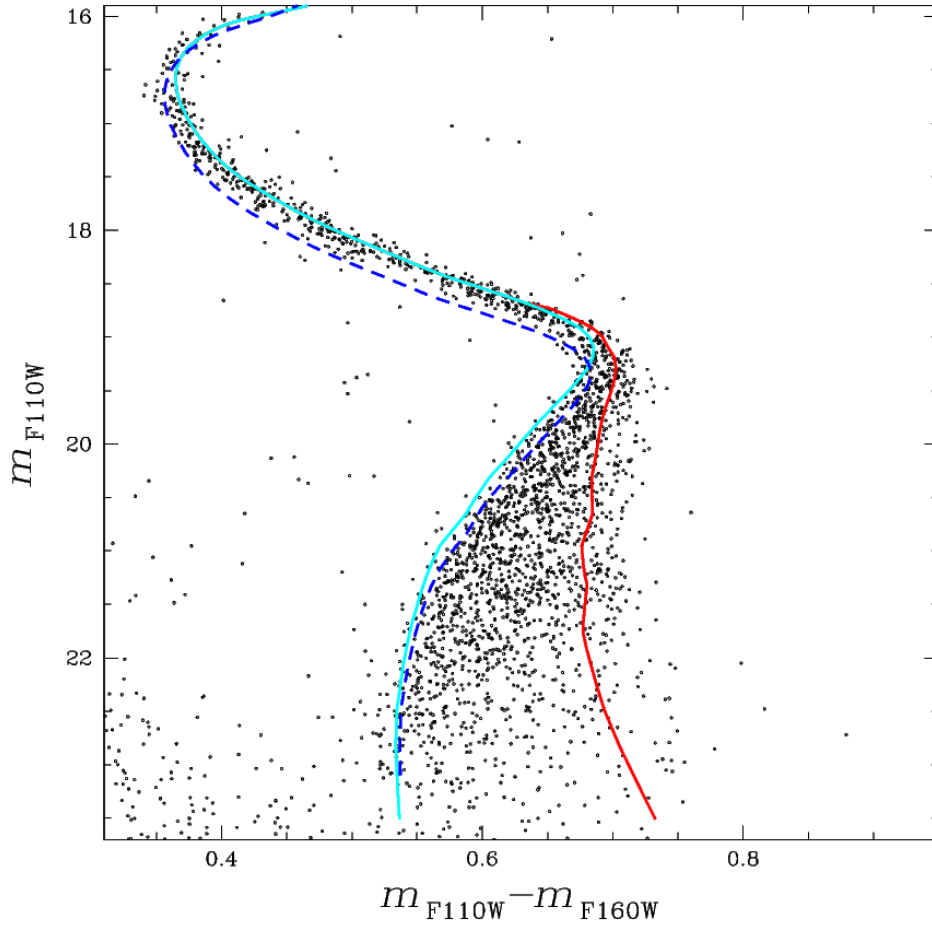
Figure 17: Comparison between the observed IR CMD and isochrones that account for the chemical composition of multiple populations (Dotter et al., 2008; Milone et al., 2023; Ziliotto et al., 2023). All isochrones have [Fe/H]=−0.7, and [α/Fe]=0.4. I adopt an age of 12 Gyr, reddening E(B−V)=0.01 mag and distance modulus $(m - M)_0$=13.21 mag. The azurre and blue-dashed isochrone share the same chemical composition but different helium abundances of Y=0.256 and Y=0.33, respectively. The red isochrone has Y=0.256 but is depleted in oxygen by 0.6 dex with respect to the other isochrones.

and 2G stars correspond to distinct stellar generations, the chemical composition of the 2G would not depend on stellar mass. Indeed, in these scenarios 1G and 2G stars originated from distinct clouds and their [O/Fe] values reflect the chemical composition from which massive and low-mass stars born alike.

On the contrary, the scenarios based on accretion can predict that the amount of polluted material is proportional to the stellar mass (e.g. Gieles et al., 2018; Bastian et al., 2013). These scenarios suggest that all GC stars (i.e. both 1G and 2G

stars) formed at the same time from the same interstellar medium. The chemical composition of the so called 2G stars is due to accretion of material processed by massive stars by already formed pre-MS GC 1G stars. In case of Bondi-like accretion, we expect that the amount of oxygen that is accreted by the 2G stars is proportional to the square of the stellar mass. As a consequence, the maximum oxygen variation observed among very-low-mass stars would be significantly smaller than that observed among the more-massive RGB stars. Clearly, the results of this thesis corroborate the evidence that the maximum oxygen variation does not depend on stellar mass, thus challenging formation scenarios based on accretion of polluted material into pre-existing stars (Gieles et al., 2018; Bastian et al., 2013).

3.3 The Chromosome Map

To further investigate the multiple populations in 47 Tucanae, I used the m_{F110W} vs. $m_{F110W} - m_{F160W}$ and the m_{F110W} vs. $m_{F606W} - m_{F110W}$ CMDs. The reason why $m_{F110W} - m_{F160W}$ is an efficient color to disentangle multiple stellar populations among M-dwarfs in GCs is that the F160W band of IR/WFC3 is strongly affected by molecules that contain oxygen, including water. On the contrary, the F110W band is poorly affected by these molecules. As a consequence 2G stars, which are oxygen poor, are brighter in F160W and redder in F110W$-$F160W, compared to 1G stars (Milone et al., 2012). Similar to F160W, the F606W filter is also affected by molecules that involve oxygen in metal-rich GCs. For this reason, the F606W$-$F110W color provides an additional tool to identify 1G and 2G stars in 47 Tucanae (Milone et al., 2023). In the following I combine these two CMDs to gather information on multiple populations in 47 Tucanae by using the Chromosome Map.

The ChM of a GC is a pseudo color diagram that aims at maximizing the separation in chemical abundances for different stellar populations. Historically, most ChMs are constructed with multi-band photometry in the F275W, F336W, F438W, and F814W of *HST* (Milone et al., 2015; Lagioia et al., 2021) or with U, B, I photometry from ground-based facilities (Jang et al., 2022).

The main limitation of the traditional ChMs: they involve photometry in UV filters which can be derived for bright stars only, including RGB, AGB, and bright MS stars. Hence, stars with masses below $0.6_\odot$ are poorly explored in the context of multiple populations because it is not possible to derive precise UV photometry with the present-day facilities.

To overcome this limitation, in this thesis I exploit a new ChM which is obtained from optical and near-infrared photometry and is sensitive to stellar populations among M-dwarfs (Milone et al., 2023).

Specifically, I use deep photometry in the F606W band of UVIS/WFC3 and the F110W and F160W bands of NIR/WFC3.

The method for deriving the ChM from the $m_{F606W} - m_{F110W}$ and $m_{F110W} - m_{F160W}$ colors, is similar to the procedure adopted for the traditional ChMs (Milone et al., 2015, 2017b, and references therein).

The very first step is the cross-identification of stars measured in the catalogs derived from F606W, F110W, and F160W images.

To do this, I use the computer program *xym1mat* (Anderson & King, 2000)

and derived the six-parameter linear transformations that convert the coordinates of the stars measured in the F606W and F160W images into the reference frame derived for the F110W filter.

To exclude most mismatched stars and sources with poor astrometry and photometry, I limited the analysis to the stars that satisfy the condition: $\sqrt{\delta x^2 + \delta y^2} <$ 0.5 pixel, where δx and δy are the difference between the position of a star measured in the F110W and in the F606W (or F160W) images, after being transformed in the same reference frame. The selected stars comprise the $\sim 95\%$ of the total number of stars brighter than $m_{\mathrm{F110W}} = 23.0$ mag.

The next step in constructing the ChM is to set the red and blue boundaries of the MS.

In this work, I derived the ChM for stars with F110W mag between 19.9 and 22.4, where the multiple stellar populations are clearly visible in both CMDs. Then I trace two fiducial lines that mark the red and blue boundary of each CMD. To derive them I used a procedure based in part on the naive estimator (Silverman, 2018). I started by dividing the MS into F110W magnitude bins of size δ_{m}=0.5 mag. The bins are defined over a grid of points separated by intervals of fixed magnitude (s = $\delta_{\mathrm{m}}/3$). For each magnitude bin I calculated the value of the 4th and the 96th percentile of the $m_{\mathrm{F110W}} - m_{\mathrm{F160W}}$ and $m_{\mathrm{F606W}} - m_{\mathrm{F110W}}$ color distributions, to which I associated the mean F110W magnitude of MS stars in each bin. As an example, these points are colored red and blue in the m_{F110W} vs. $m_{F110W} - m_{F160W}$ CMD of Figure 18. The resulting envelope of the MS is provided by the red and blue lines of Figure 18.
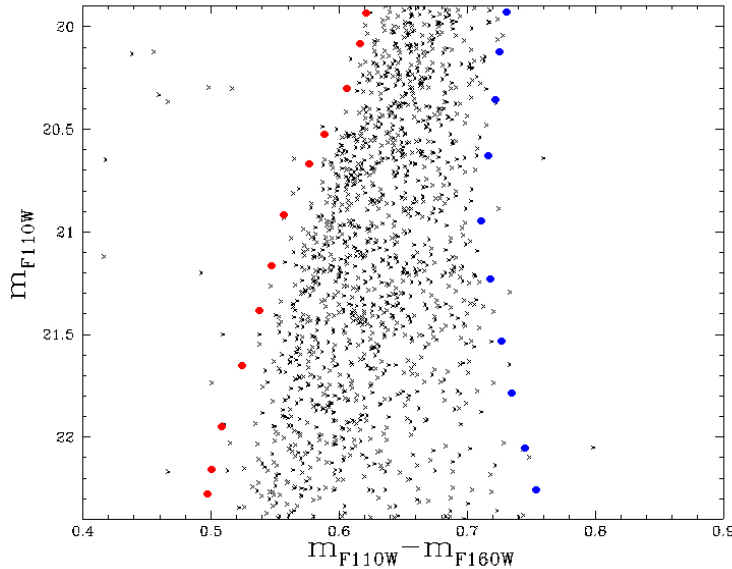

Figure 18: m_{F110W} vs. $m_{F110W} - m_{F160W}$ CMD for stars in the Sector A, zoomed around the MS region below the knee. The red and blue dots mark the red and blue boundaries of the MS and are used to derive the ChM. See the text for details.

The fiducial lines are then used to verticalize the CMDs, and derive the m_{F110W} vs. $\Delta_{F110W-F160W}$ diagram plotted in Figure 19. Do to this, I used the following relation:
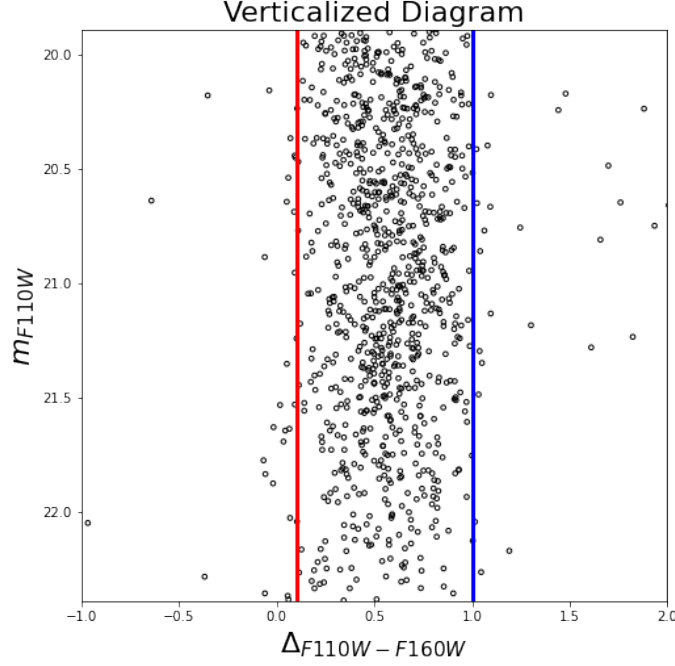

Figure 19: $\Delta_{F110W-F160W}$ vs m_{F110W} verticalized diagram

$$\Delta_{F110W-F160W} = \frac{X_R - X}{X_R - X_B}$$

Where:

- X defines the $m_{\mathrm{F110W}} - m_{\mathrm{F160W}}$ color of the target star

- X_R defines the color of the red fiducial line, at the same F110W magnitude of the target star. In this context, the red fiducial line defines the rightmost boundary of the CMD.

- X_B defines the color of the blue fiducial at the same F110W magnitude of the target star. In this context, the blue fiducial line defines the leftmost boundary of the CMD.

The same process was repeated for the m_{F110W} vs $m_{F606W} - m_{F110W}$ CMD, from which I derived the pseudo color.

$$\Delta_{F606W-F110W} = \frac{X - X_R}{X_R - X_B}$$

Plotting the previously derived pseudo-colors in relation to each other yields the ChM of M-dwarfs shown in Figure 20. In the next Chapter I use this ChM to gain information on multiple populations in 47 Tucanae.
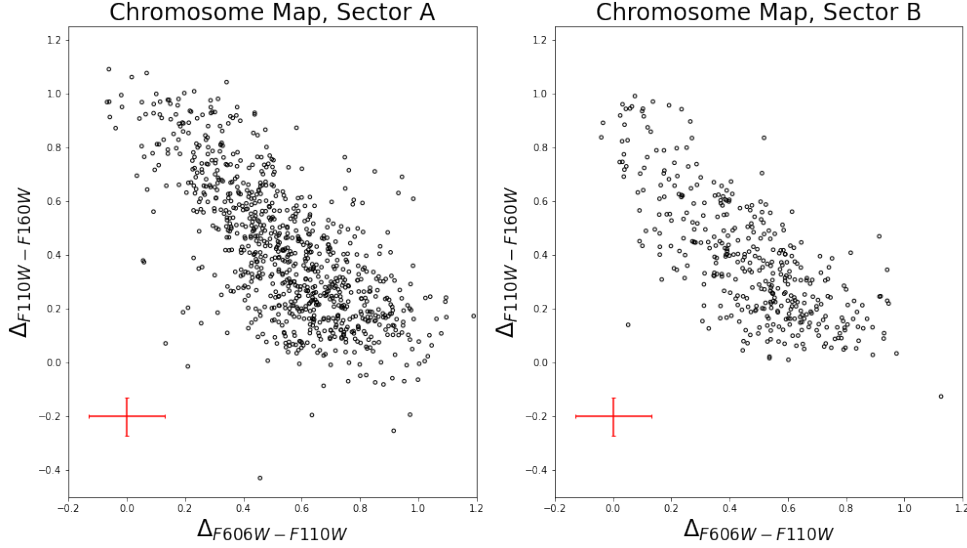

Figure 20: $m_{F606W} - m_{F110W}$ vs. $m_{F110W} - m_{F160W}$ ChMs for M-dwarfs in Sector A (left) and B (right). The average error bars are marked in red.

I present the Gaussian Filter image in Figure 21 to emphasize the density of star distribution in the ChM. In Figure 21 I observe two main conglomerations, with minor fluctuations around 1G and an extension in 2G.

First I calculated the frequency of data distribution. Each pixel within an image carries a value, representing the number of stars within its domain. Subsequently, am image enhancing technique sourced from *scipy* python library is employed. Gaussian Filter is a method based on convolving the input image with a Gaussian Kernel. A Gaussian kernel, in this context, refers to a 2D Gaussian distribution. The smoothing is characterized by σ, the standard deviation for Gaussian kernel. Opting for a larger value leads to the loss of main structures while a small σ is highly sensitive to noise. The choice of $\sigma = 3.5$ in this thesis is an empirical compromise between the two extremes.

The contours were detected through *find_contours* python function from the *skimage* library, based on Marching Squares Algorithm (MSA). It is a 2D case of marching cubes algorithm, commonly used to mark altitude in topological maps.

In the MSA a sub-grid of one pixel iterates through the image, rotating clockwise at each iteration. Based on a vertex value of the sub-grid, each pixel is assigned a binary value that corresponds to a certain configuration. All possible cases are
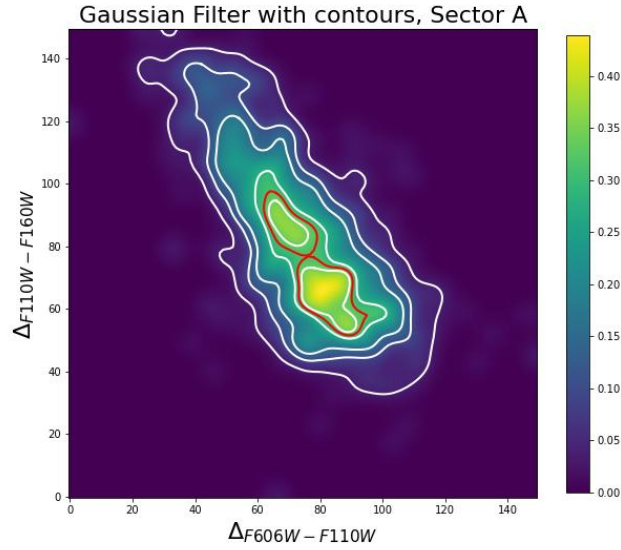
Figure 21: $m_{F606W} - m_{F110W}$ vs. $m_{F110W} - m_{F160W}$ ChM for Sector A with Gaussian filter applied. In white are detected contours, in red - intersecting contours. See the text for more details.

listed in Figure 22. It is then possible to trace these configurations through an image to construct a contour.
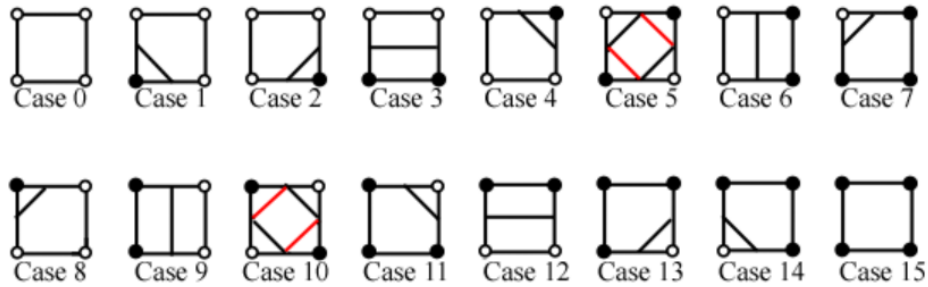

Figure 22: MSA algorithm sub-grid possible configurations from d'Azur (2023)

To produce the contours in Figure 21 I have iterated the MSA algorithm through various brightness levels of the image.

4 Results and discussion

In this Chapter, I first discuss the ChMs of 47 Tucanae and investigate its multiple populations of very-low-mass stars. After combining my results with existing literature, I discuss the radial distributions of both high- (~ 0.8 M$_\odot$) and low-mass ($\sim 0.2 - 0.4$ M$_\odot$) stars.

To derive the ChM of M-dwarfs, I plot the pseudo-color $\Delta_{F110W,F160W}$ as a function of $\Delta_{F606W,F110W}$.

The results are plotted in Figure 23, where I show the ChMs of stars in Sectors A and B with the corresponding $\Delta_{F606W-F110W}$ and $\Delta_{F110W-F160W}$ histogram distributions.
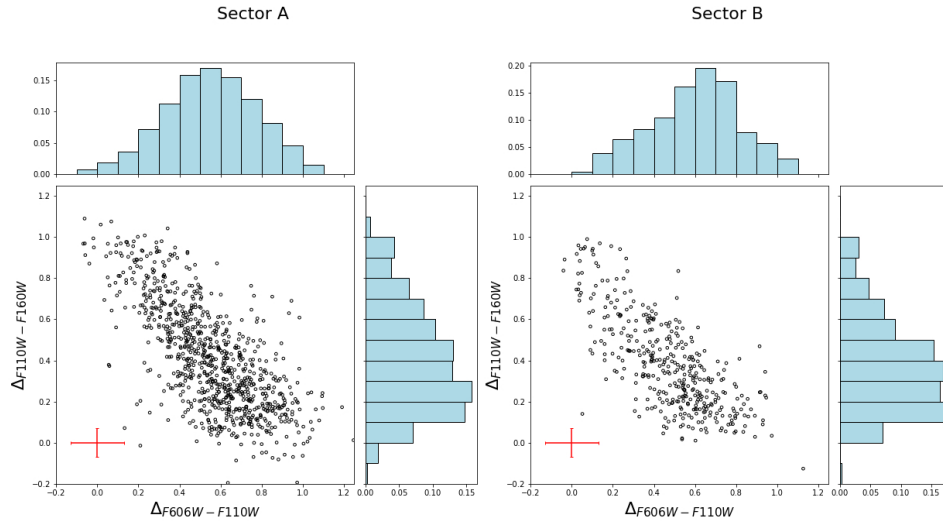

Figure 23: $\Delta_{F110W-F160W}$ vs. $\Delta_{F110W-F160W}$ ChMs and number distribution histograms of $\Delta_{F606W-F110W}$ and $\Delta_{F110W-F160W}$. Left and right panels refer to Sector A and B, respectively.

To better interpret the position of the stars along the ChM, I simulate a ChM for a simple stellar population using the same number of stars and observational errors as for 47 Tucanae stars. As illustrated in Figure 24, the simulated stars (aqua triangles) distribute around the position with ($\Delta_{F110W-F160W}$,$\Delta_{F110W-F160W}$) = (0.8,0.2). These stars account for the distribution of the observed 1G stars. Whereas the 2G stars define the extended sequence with $\Delta_{F110W,F160W} > 0.3$ mag. Based on the distribution of simulated stars, I derived by eye the red dashed line, which separates the bulk of 1G stars (located below the line) from the 2G (above the line).

I notice an extended 1G sequence in the ChM, similar to what is observed in RGB stars (Milone et al., 2017a; Jang et al., 2022). Indeed, the $\Delta_{F606W,F110W}$ pseudo-color extension is wider than that expected from observational errors alone. Based on the comparison between the observed ChM and ischrones from the Dartmouth database (Dotter et al., 2008) the extended 1G sequence in the ChM is
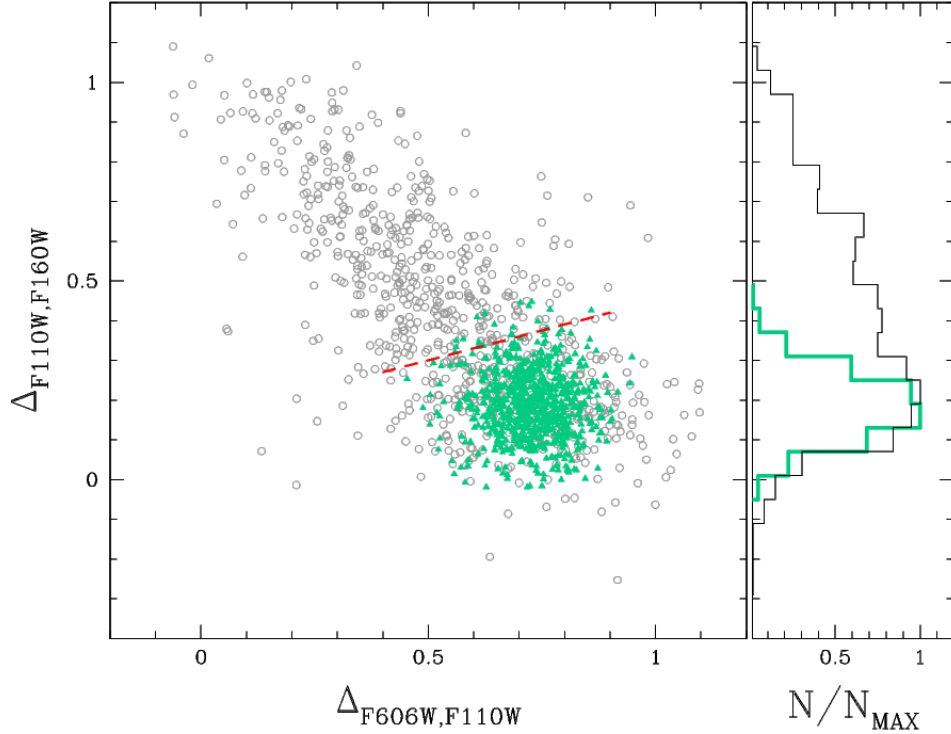
Figure 24: Comparison of the simulated (aqua triangles) and observed (gray circles) $\Delta_{F110W-F160W}$ vs. $\Delta_{F110W-F160W}$ ChMs of stars in Sector B.

consistent with star-to-star metallicity variations among 1G stars of the order of [Fe/H]$\sim$0.1 dex, in close analogy with what was previously observed from *HST* and *JWST* photometry (Milone et al., 2023; Legnardi et al., 2022) and high-resolution spectroscopy from the Very Large Telescope (Marino et al. 2023).

The comparison of the $\Delta_{F110W,F160W}$ histogram distributions of stars in Sector A and B provides information on multiple populations at different radial distances from the cluster center.

Both histograms exhibit a main peak around $\Delta_{F110W,F160W} \sim 0.3$ mag, which is mostly due to 1G stars, and a tail of stars that extends towards larger values of $\Delta_{F110W,F160W}$, composed of 2G stars. The 2G stars with extreme chemical composition populate the region with $\Delta_{F110W,F160W} > 0.7$ mag (see also Milone et al. 2023).

To compare the distributions of stars in the sectors A and B, I normalized both histograms to the same number of stars and subtracted the histogram of Sector B from that of Sector A. The results are illustrated in Figure 25, where I plot the residuals as a function of $\Delta_{F110W,F160W}$.

I notice negative residuals among the stars with $\Delta_{F110W,F160W} \leq 0.4$ mag, which correspond to the 1G, and positive residuals for stars with $\Delta_{F110W,F160W} > 0.4$ mag, i.e. 2G stars. These results indicate the lack of evidence for a large gradi-
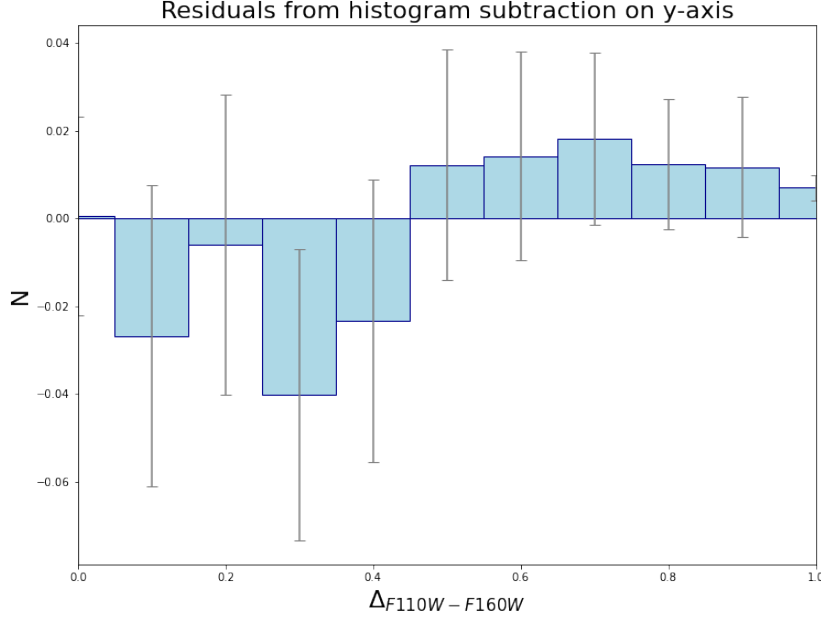
Figure 25: Residuals of histogram subtraction of Sector B from Sector A as a function of $\Delta_{F110W,F160W}$. Errors are presented in gray

ent when moving from sector A to sector B, although there is some hint that the fraction of 2G stars decreases when moving from sector A to Sector B. Although the difference has poor statistical significance, this result corroborates similar conclusion by Dondoglio et al. 2021 based on HB stars that the population ratio outside 6 arcmin from the cluster center could be not constant, but exhibit a small gradient.

Intriguingly, there is no significant difference between the residuals of 2G stars with extreme and intermediate chemical composition.

To quantify the fraction of 1G and 2G stars we extended the method used in various papers (e.g. Milone et al. 2012; Nardiello et al. 2018; Zennaro et al. 2019) to the ChM of 47 Tucanae. The procedure is illustrated in Figures 26 and 27.

Briefly, I defined three regions in the ChM, namely R1, R2A, and R2B. Region R1 comprises the bulk of 1G stars and consists in the ChM portion below the dashed-red line. R2A and R2B are separated by the blue dashed line, which is derived with the criterium of including a simple stellar population based on the distribution of photometric uncertainties. I indicate 2GA, the sample of 2G stars below the blue line, whereas the remaining 2G stars are named 2GB.

I calculated the average values of $\Delta_{F606W,F110W}$ and $\Delta_{F110W,F160W}$ for the stars of regions R1 and R3 (aqua dots in Figure 27) and used these points as centers of these regions, which I associated with a simple population. To reproduce the continuous distribution of stars in the region R2, I assumed that population 2GA
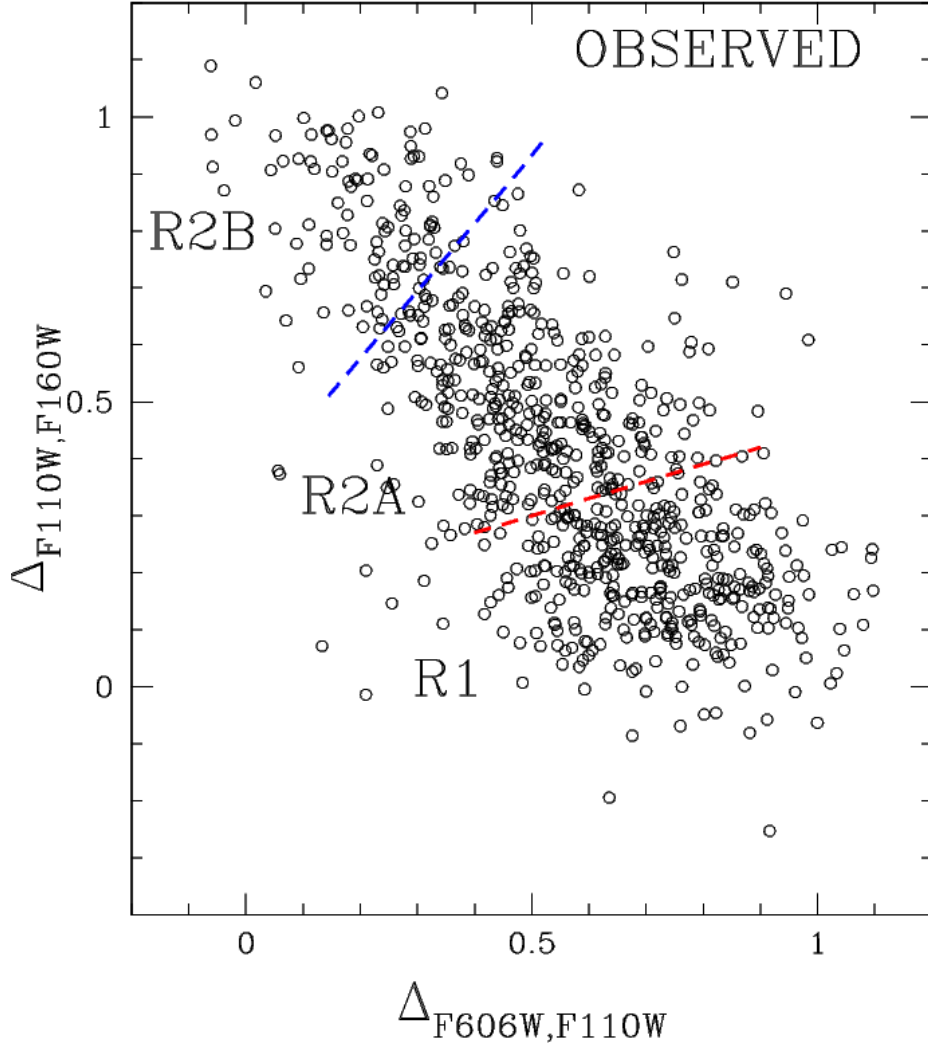
Figure 26: Reproduction of the $\Delta_{\mathrm{F110W,F160W}}$ vs. $\Delta_{\mathrm{F606W,F110W}}$ ChM for stars in Sector A. The red and blue dashed lines separate the three regions of the ChM, R1, R2A, and R2B, which are mostly populated by 1G, 2GA, and 2GB stars, respectively, and that I used to estimate the fraction of stars in each population.

is composed of three simple stellar sub-populations with different centers. The centers of each population are marked with aqua dots in Figure 27.

Due to observational errors, each region can include stars of the other populations. Specifically, the observed number of stars within the region R1 is:

$$NR1 = N_{1G}f_{1G}^{R1} + N_{2GA}f_{2GA}^{R1} + N_{2GB}f_{2GB}^{R1} \tag{3}$$

where $N_{1G(2GA,2GB)}$ is the total number of analyzed 1G (2GA, 2GB) stars and $f_{1G(2GA,2GB)}^{R1}$ is the fraction of 1G (2GA, 2GB) stars in the region R1. The number

of observed stars in the regions R2A and R2B are related to the fractions of stars of each population by two similar equations.

By solving these three equations I estimate the total numbers of 1G, 2GA, and 2GB stars and the corresponding fractions with respect to the total number of studied MS stars. The results can be summarized by introducing the following notation:

- N_{tot}^A is the total number of stars in the ChM in Sector A and is equal to 863

- N_{2G}^A/N_{tot}^A defines the fraction of 2G stars in Sector A and is equal to 0.570 ± 0.018. This value is comparable with the fraction of stars in the regions R2A and R2B of the ChM (0.561 ± 0.017).

- N_{tot}^B is the total number of stars in the ChM in Sector B (Figure 20 Right Panel) and equals to 385

- N_{2G}^B/N_{tot}^B defines the fraction of 2G stars in Sector B and is equal to 0.549 ± 0.024, which is comparable with the fraction of stars in the region R2A and R2B of the ChM (0.553 ± 0.026). Hence, I conclude that the fraction of 2G stars is constant in the two sectors is significant at 1σ value, although our results, together with previous findings by Dondoglio et al. 2021 based on red-HB stars hint at a slight decrease in the fraction of 2G stars when moving from ~6 arcmin to the cluster outskirts.

- The 2GB stars comprise the $12.9\pm2.0\%$ and the $13.5\pm3.5\%$ of the total number of stars in Sector A and B, respectively.

These results confirm the qualitative conclusion based on the comparison of the histogram distributions of stars in the ChMs of Sector A and B.

A visual inspection of the ChM of M-dwarfs reveals that there is no sharp separation between 1G and 2G stars, in contrast with what is observed along the RGB and the upper MS where 1G and 2G stars define two discrete groups of stars in the traditional ChM (e.g.Milone et al. 2017a). The simulations are plotted in Figure 27, where I used discrete groups of stars, required that the sub-population of 2G stars closest to the 1G has a $\Delta_{F110W,F160W}$ difference of 0.2 dex with respect to the 1G, which would correspond to a difference of [O/Fe]=0.09 dex, based on the isochrones by (Milone et al. 2023, see Chapter 3).

I suggest that, if the 1G and 2G stellar populations of 47 Tucanae have discrete oxygen abundances, such difference should be of the order of 0.1 dex or smaller. Although the physical reasons responsible for the possible absence of discrete stellar populations among M-dwarfs are still unclear (e.g Ziliotto et al. 2023, but see also discussion by Renzini et al. 2015 on the evidence of discrete MSs in the CMDs but continuous stellar distributions along the Na-O anticorrelation), I notice that the traditional ChMs, used to analyze MPs along the RGB and the bright MS, are mostly sensitive to stellar populations with different nitrogen abundances, whereas the ChM used in this thesis disentangles stars with different oxygen content. Hence, our results could suggest that oxygen and nitrogen follow different distributions.
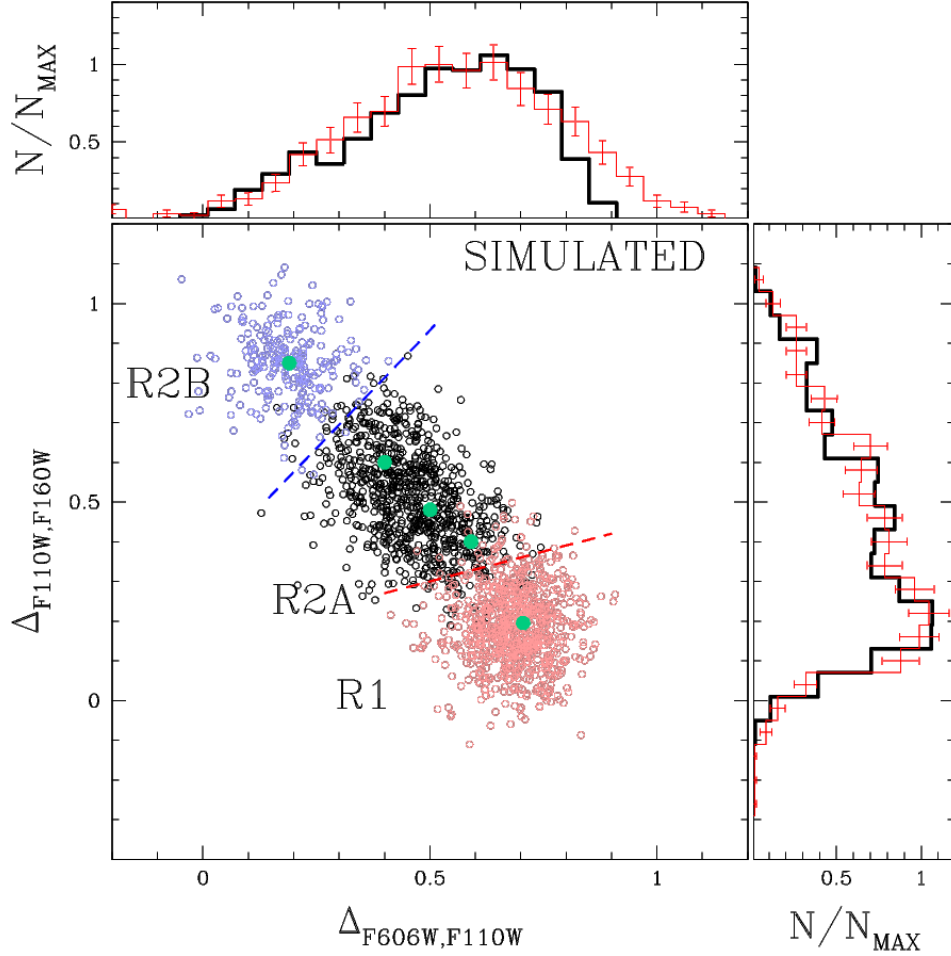
Figure 27: Illustration of the method to estimate the population ratios for stars in Sector A. The large panel is the simulated ChM, where I indicated the three regions, R1, R2A, and R2B, used to estimate the fraction of stars in each population. The simulated 1G and 2GB stars are colored red and blue, respectively, whereas 2GA stars are represented with black colors. The aqua dots are the centers of the populations. See the text for details. The top and right panels compare the histogram $\Delta_{F606W,F110W}$ and $\Delta_{F110W,F160W}$ distributions of simulated (black) and observed stars (red).

4.1 Chromosome maps that involve the F390W band

For completeness, I derived additional ChMs that include the F390W band. These include the $\Delta_{F390W-F110W}$ vs $\Delta_{F110W-F160W}$ ChM shown in Figure 29 and the $\Delta_{F390W-F110W}$ vs $\Delta_{F390W-F606W}$ ChM plotted in Figure 28. Both ChMs are derived with the same procedure illustrated for the $\Delta_{F110W,F160W}$ vs. $\Delta_{F606W,F110W}$ ChM.
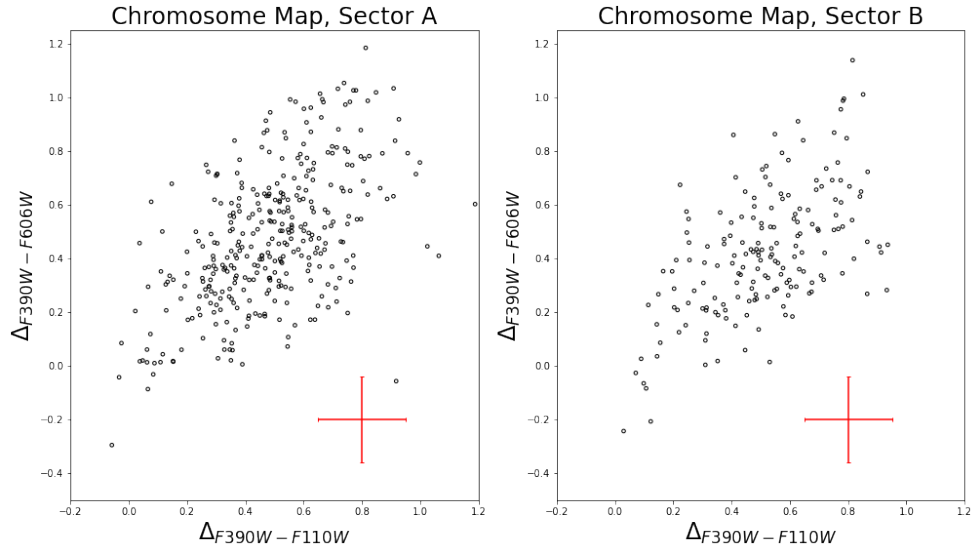
43

Figure 28: $\Delta_{F390W-F110W}$ vs $\Delta_{F390W-F606W}$ ChMs for Sector A and B. The average errors are marked in red.
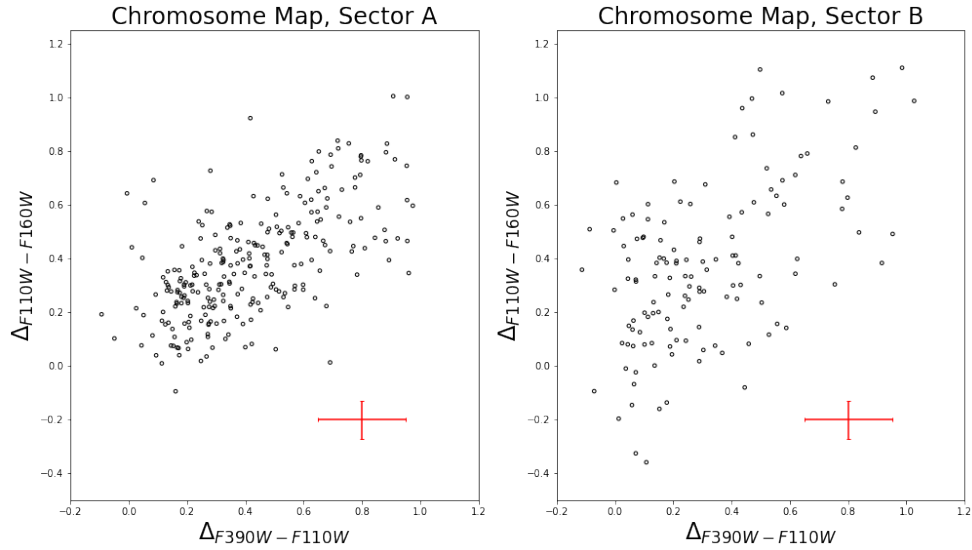

Figure 29: $\Delta_{F390W-F110W}$ vs $\Delta_{F110W-F160W}$ ChMs for Sector A and B. Error bars are marked in red.

To shed light on the distribution of 1G and 2G stars in these new ChMs, I used red and blue colors to represent the same 1G and 2G stars identified in the $\Delta_{F606W-F110W}$ vs. $\Delta_{F110W-F160W}$ ChM for stars in Sector A of Figure 30. Stars
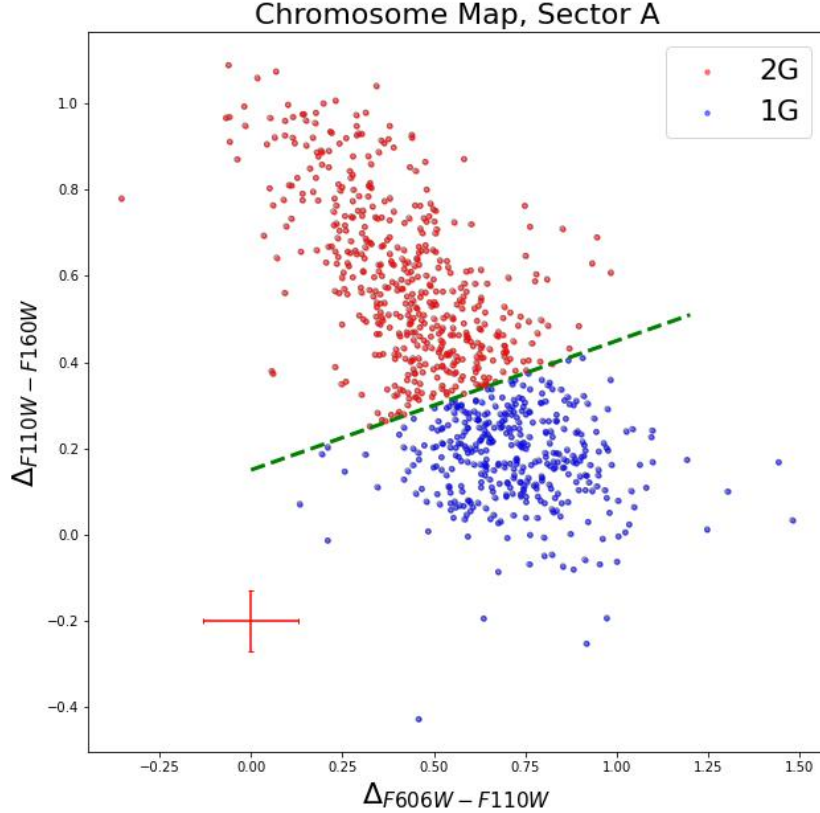
Figure 30: $\Delta_{F606W-F110W}$ vs. $\Delta_{F110W-F160W}$ ChM for stars in Sector A. The red dots and blue dots represent 2G and 1G stars, which are separated by the green dashed line. The photometric errors are displayed in red.

identified as 1G-2G from the $\Delta_{F606W-F110W}$ vs. $\Delta_{F110W-F160W}$ ChM are shown on ChMs including the F390W filter with the same color encoding (Figures 31 and 32). 1G and 2G stars appear to maintain coherent distributions in F390W filter, which suggests that it is a promising tool for future investigations of multiple populations.

Although the emphasis of this thesis is on $\Delta_{F606W-F110W}$ vs. $\Delta_{F110W-F160W}$ ChM (Figure 30), I was able to disentangle, for the first time, the main populations of 47 Tucanae with the F390W filter. Future work, based on the comparison of these new ChMs and simulated ChMs based on synthetic spectra that account for the chemical compositions of multiple populations in GCs are mandatory to interpret the results from these ChMs.
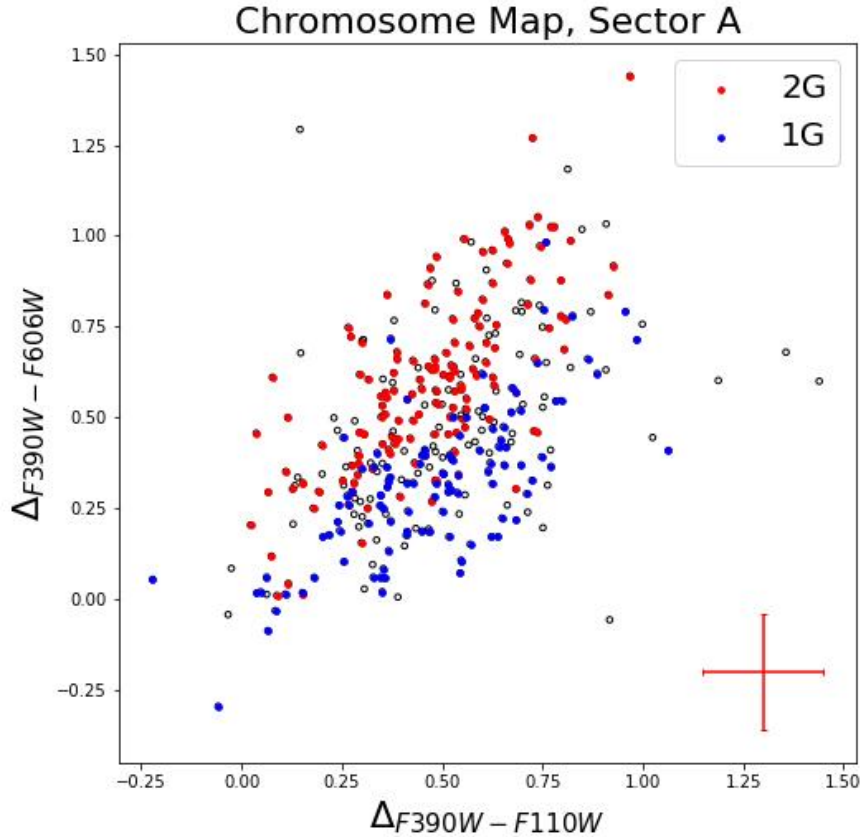
Figure 31: Reproduction of the $\Delta_{F390W-F110W}$ vs $\Delta_{F390W-F606W}$ ChMs for stars in Sector A. Blue and red colors indicate the 1G and 2G stars identified in the ChM of Figure 30.

4.2 Radial Distribution of Multiple populations among VLM stars

The radial distribution of multiple stellar populations can provide constraints on the early phases of the GC life. Indeed, star clusters with long relaxation times like 47 Tucanae, (Harris (2010) reports that the logarithm of the relaxation time of 47 Tucanae at half-light radius is 9.55) may retain some information on the initial configuration.

The radial distribution of 1G and 2G stars in 47 Tucanae was widely studied by means of multi-band photometry (both from HST and ground-based wide-field facilities, e.g. Milone et al. 2012; Dondoglio et al. 2021) and from spectroscopy (e.g. Cordero et al. 2014). It is widely accepted that 2G stars of 47 Tucanae are
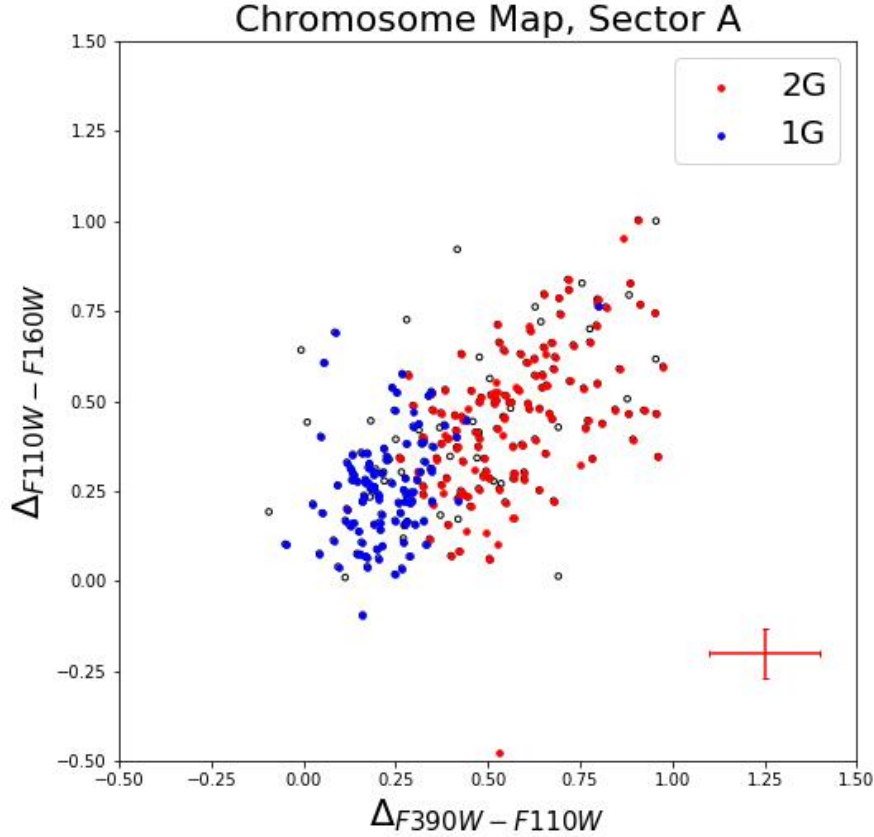
Figure 32: $\Delta_{F390W-F110W}$ vs $\Delta_{F110W-F160W}$ ChM for stars in Sector A. The red dots represent the 2G stars and the blue dots represent the 1G stars identified in the ChM of Figure 30. The photometric errors are displayed in red.

more-centrally concentrated than the 1G.

The results from literature are summarized in Figure 33, where I plot the fraction of 2G stars as a function of the radial distance from the cluster center and use the black points to reproduce the findings by Dondoglio et al. 2021. The fraction of 2G stars is $\sim 80\%$ in the cluster center and drops to $\sim 60\%$ at a radial distance of about 6 arcmin (corresponding to about 1.9 half-light radii) from the center. It remains nearly constant at larger radial distances.

However, the main limitation of these studies is that they are based on RGB and red-HB stars alone, while the low stellar mass regime is unexplored.

Here, I used the $\Delta_{F606W-F110W}$ vs $\Delta_{F110W-F160W}$ ChMs plotted in Figure 20 Left Panel and Figure 20 Right Panel to separate the bulk of 1G and 2G stars in
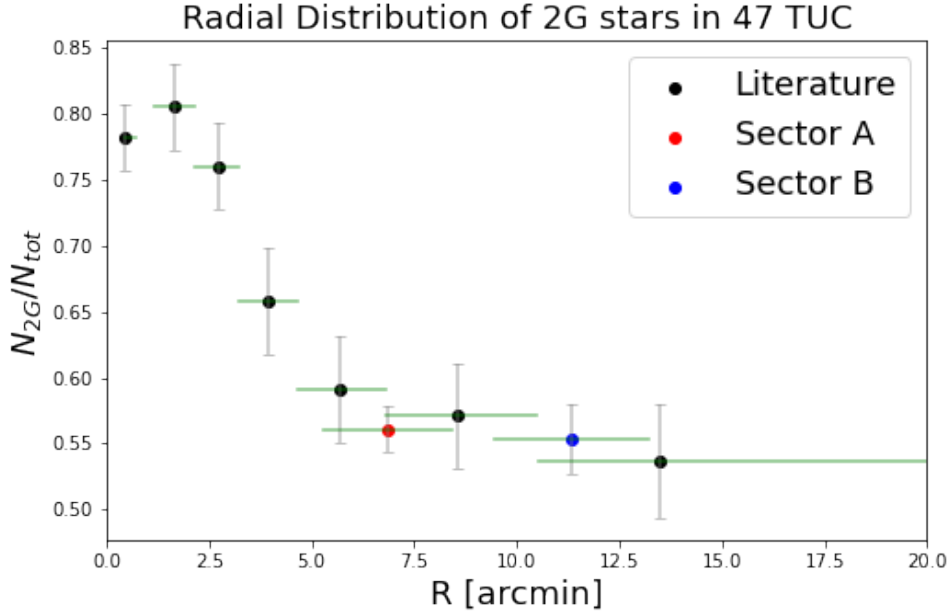
47

Figure 33: Fraction of 2G stars as a function of radial distance for 47 Tucanae. Black dots correspond to HST and ground-based photometric values from (Dondoglio et al., 2021). Gray lines mark the errors, green horizontal lines mark the extension of the radial interval. The red dot indicates the data from Sector A, the blue dot corresponds to Sector B

Sectors A and B respectively, and infer the fraction of 2G stars among M-dwarfs.

To quantify the radial distribution of multiple populations I use the fractions of 2G stars derived above, which are represented with colored dots in Figure 33.

The fractions of 2G stars derived from my analysis on M-dwarfs are represented with red and blue symbols in Figure 33. Noticeably, the fraction of 2G stars in both sectors A and B is nearly the same, and is consistent with the values derived from RGB and red-HB stars with similar radial distances from the cluster center.

The evidence that the 2G stars of 47 Tucanae are more centrally concentrated than 1G is consistent with the formation scenarios where the 2G stars of GCs form in the innermost cluster regions (e.g. D'Ercole et al. 2010; D'Antona et al. 2016; Renzini et al. 2016 and references therein). Although the dynamical evolution drives 1G and 2G stars to mix, in GCs like 47 Tucanae, which are dynamically young, 2G stars retain the information of their initial configuration.

The fact that VLM stars and their massive counterparts in 47 TUC share a comparable radial distribution challenges the accretion scenario. This is due to the fact that accretion scenario suggests that VLM stars would be less efficient in accreting polluted material. Hence, we could expect a smaller fraction of 2G stars among VLM stars.

(Vesperini et al., 2018) employs N-body simulations to investigate the evolution

of the mass functions of multiple populations in globular clusters in the context of the multiple-generation scenarios. In cases when 2G and 1G formed with the same initial mass function and 2G stars were more centrally concentrated, their simulations show that small differences arise in the local and global present-day mass function due to dynamical evolution. However, in more advanced stages of evolution, when 1G and 2G are mixed, these dynamically-induced differences disappear. At the same time, if 1G and 2G form with strikingly different initial mass functions, the simulations by Vesperini and collaborators predict large differences in the mass function. These differences increase for dynamically old clusters.

The finding that the fraction of 1G and 2G stars among stars with different masses are constant, is consistent with the idea that the two stellar populations share the same present-day mass functions and, according to the simulations by (Vesperini et al., 2018), the same initial mass functions. Similar conclusions that 1G and 2G stars share the same mass functions are provided for NGC 6752, M 4, and NGC 2808 by Milone et al. 2019 and Dondoglio et al. 2021.

At the same time, the central concentration of 2G stars that we observed in 47 Tucanae would imply that 2G stars formed in the center of the GC in a high-density environment, as predicted by the multiple-generation scenarios.

As a consequence, I suggest that the initial mass function could not depend on stellar density, hinting at the fact that the initial mass function is a universal property of star formation.

5 Conclusion

In this thesis, I analyzed multi-band deep photometry of stars in two external regions of the GC 47 Tucanae.

I have used the computer programs and the methods developed by Jay Anderson to derive high-precision astrometry and photometry in the F390W and F606W bands of UVIS/WFC3 and the F110W and F160W filters of IR/WFC3. The resulting CMDs comprise stars that span various evolutionary sequences, including the red HB, RGB, SGB, MS, and the white dwarf cooling sequence. The comparison between the CMD derived from IR photometry and the isochrones from Dotter et al. 2008 reveals that the faintest MS stars I detected have masses smaller than $\sim 0.1\ M_\odot$, which is the faintest mass limit of the available isochrones.

The main results can be summarized as follows:

- The m_{F160W} vs. $m_{F110W} - m_{F160W}$ CMD reveals that the MS region between the SGB and the knee is narrow and well defined and its width is comparable with the color and magnitude broadening due to observational uncertainties alone. On the contrary, the M-dwarfs fainter than the MS knee exhibit a wide $m_{F110W} - m_{F160W}$ color range that is much wider than that expected by the errors. I conclude that the observed color broadening is consistent with multiple stellar populations of very-low-mass stars with different chemical compositions. Similar conclusions are derived from the m_{F390W} vs. $m_{F390W} - m_{F606W}$ and the m_{F110W} vs. $m_{F110W} - m_{F160W}$ CMDs.

- The comparison between isochrones that account for different light-element abundance variations and the m_{F160W} vs. $m_{F110W} - m_{F160W}$ CMD shows that the wide color distribution of M-dwarfs is consistent with star-to-star oxygen variation by [O/Fe]~ 0.6 dex. Such value is similar to the maximum oxygen variation detected among RGB stars by means of high-resolution spectroscopy (e.g. Carretta et al. 2009). I conclude that there is no evidence for a significance difference between the relative oxygen abundances of M-dwarfs (M$\sim$0.2-0.4M$_\odot$) and the more-massive (M$\sim$0.8M$_\odot$) RGB stars.

- To combine the information on multiple populations from different CMDs, I constructed the $\Delta_{F110W,F160W}$ vs. $\Delta_{F606W,F110W}$ ChM. The ChM allowed me to disentangle the bulk of 1G stars from the 2G. The latter defines an extended sequence in the ChM, thus revealing at least two groups of 2G stars, namely 2GA and 2GB, with intermediate and extreme oxygen abundances. The 2G stars comprise about $\sim$55% of the total number of studied stars, and their fraction is nearly constant in the two analyzed fields. Similarly, there is no significant difference between the fractions of 2GA and 2GB stars in Sectors A and B. The fraction of 2G stars that I measured among M-dwarfs is comparable with that of RGB and red HB stars at similar radial distances and is significantly smaller than that observed in the innermost cluster regions where the 2G comprises up of $\sim$80% of the total number of cluster members (e.g. Milone et al. 2012; Dondoglio et al. 2021; Cordero et al. 2014). Our results, together with the findings from the literature, corroborate the evidence of a strong gradient of the fraction of 2G stars in 47 Tucanae.

- Finally, I report the first investigation of ChMs of M-dwarfs involving F390W filter, $\Delta_{F390W-F110W}$ vs $\Delta_{F110W-F160W}$ and the $\Delta_{F390W-F110W}$ vs $\Delta_{F390W-F606W}$. Both ChMs allows the identification of 1G and 2G stars, demonstrating that photometry in the F390W filter is an efficient tool to identify multiple populations among very-low-mass stars. Further investigation based on the comparison of these new ChMs and simulated ChMs derived from synthetic photometry that accounts for various chemical compositions of 1G and 2G stars will allow me to understand the physical reason that determine the location of 1G and 2G stars in these ChMs.

The results of this thesis provide observational constraints to the formation scenario of multiple populations formation in GCs. The evidence of a strong gradient of the fraction of 2G stars together with the finding that 1G and 2G of stars with different masses share similar oxygen abundances and relative numbers is consistent with the predictions of the formations where GCs have experienced multiple bursts of star formation and 2G formed in a dense environment in the innermost cluster regions (e.g. D'Ercole et al. 2010; D'Antona et al. 2016; Renzini et al. 2022 and references therein).

References

Anderson J., 2022, Instrument Science Report WFC3, 2022-5, 55

Anderson J., Bedin L. R., 2010, Publications of the Astronomical Society of the Pacific, 122, 1035

Anderson J., King I., 2000, Publications of the Astronomical Society of the Pacific, 112, 1360

Anderson J., et al., 2008, The Astronomical Journal, 135, 2114

Bastian N., Lamers H. J. G. L. M., de Mink S. E., Longmore S. N., Goodwin S. P., Gieles M., 2013, Monthly Notices of the Royal Astronomical Society, 436, 2398

Calamida A., et al., 2022, The Astronomical Journal, 164, 32

Carretta E., Gratton R. G., Bragaglia A., Bonifacio P., Pasquini L., 2004, Astronomy & Astrophysics, 416, 925

Carretta E., Bragaglia A., Gratton R., D'Orazi V., Lucatello S., 2009, Astronomy and Astrophysics, 508, 695

Cordero M. J., Pilachowski C. A., Johnson C. I., McDonald I., Zijlstra A. A., Simmerer J., 2014, Astrophysical Journal, 780, 94

Criscienzo M. D., Ventura P., D'Antona F., Milone A., Piotto G., 2010, Monthly Notices of the Royal Astronomical Society, 408, 999

Denissenkov P. A., Hartwick F. D. A., 2013, Monthly Notices of the Royal Astronomical Society, pp 1–5

Dondoglio E., Milone A. P., Lagioia E. P., Marino A. F., Tailo M., Cordoni G., Jang S., Carlos M., 2021, Astrophysical Journal, 906, 76

Dondoglio E., et al., 2022, arXiv preprint arXiv:2201.08631

Dotter A., Chaboyer B., Jevremović D., Kostov V., Baron E., Ferguson J. W., 2008, The Astrophysical Journal Supplement Series, 178, 89

D'Antona F., Vesperini E., D'Ercole A., et al., 2016, Monthly Notices of the Royal Astronomical Society, 458, 2122

D'Ercole A., D'Antona F., Ventura P., Vesperini E., McMillan S., 2010, Monthly Notices of the Royal Astronomical Society

Gieles M., et al., 2018, Monthly Notices of the Royal Astronomical Society, 478, 2461

Harris W. E., 2010, arXiv preprint arXiv:1012.3224

Jang S., et al., 2022, Monthly Notices of the Royal Astronomical Society, 517, 5687

Klioner S., et al., 2022, Astronomy & Astrophysics, 667, A148

Krause M., Charbonnel C., Decressin T., Meynet G., Prantzos N., 2013, Astronomy and Astrophysics, 552, A121

Lagioia E., et al., 2021, The Astrophysical Journal, 910, 6

Legnardi M., et al., 2022, Monthly Notices of the Royal Astronomical Society, 513, 735

Legnardi M., et al., 2023, Monthly Notices of the Royal Astronomical Society, 522, 367

Marino A. F., Villanova S., Piotto G., Milone A. P., Momany Y., Bedin L. R., Medling A. M., 2008, Astronomy and Astrophysics, 490, 625

Marino A. F., et al., 2016, Monthly Notices of the Royal Astronomical Society, 459, 610

Milone A. P., Marino A. F., 2022, Universe

Milone A. P., et al., 2012, The Astrophysical Journal, 744, 58

Milone A., et al., 2013, The Astrophysical Journal, 767, 120

Milone A. P., et al., 2015, The Astrophysical Journal, 808, 51

Milone A. P., et al., 2017a, Monthly Notices of the Royal Astronomical Society, 464, 3636

Milone A. P., et al., 2017b, Monthly Notices of the Royal Astronomical Society, 469, 800

Milone A. P., et al., 2019, Monthly Notices of the Royal Astronomical Society, 484, 4046

Milone A. P., et al., 2023, Monthly Notices of the Royal Astronomical Society, 522, 2429

Nardiello D., et al., 2018, Monthly Notices of the Royal Astronomical Society, 477, 2004–2019

Nataf D. M., Gould A., Pinsonneault M. H., Stetson P. B., 2011, The Astrophysical Journal, 736, 94

Norris J. E., 2004, The Astrophysical Journal, 612, L25

Piotto G., et al., 2007, The Astrophysical Journal, 661, L53

Renzini A., et al., 2016, Monthly Notices of the Royal Astronomical Society, 459, 3635

Renzini A., Marino A. F., Milone A. P., 2022, arXiv preprint arXiv:2203.03002

Sabbi E., et al., 2016, The Astrophysical Journal Supplement Series, 222, 11

Silverman B. W., 2018, Density estimation for statistics and data analysis. Routledge

Sirianni M., et al., 2005, Publications of the Astronomical Society of the Pacific, 117, 1049

Tailo M., et al., 2020, Monthly Notices of the Royal Astronomical Society, 498, 5745

Vesperini E., Hong J., Webb J. J., D'Antona F., D'Ercole A., 2018, Monthly Notices of the Royal Astronomical Society, 476, 2731

Ye C. S., Kremer K., Rodriguez C. L., Rui N. Z., Weatherford N. C., Chatterjee S., Fragione G., Rasio F. A., 2022, The Astrophysical Journal, 931, 84

Zennaro M., Milone A., Marino A., Cordoni G., Lagioia E., Tailo M., 2019, Monthly Notices of the Royal Astronomical Society, 487, 3239

Ziliotto T., et al., 2023, arXiv preprint arXiv:2304.06026

d'Azur U. C., 2023, Matching Squares Algorithms, `http://users.polytech.unice.fr/~lingrand/MarchingCubes/algo.html`

de Mink S. E., Pols O. R., Langer N., Izzard R. G., 2009, Astronomy and Astrophysics, 507, L1

Acknowledgements